



Diquark Correlators and Phase Structure in the Quark-Meson-Diquark Model beyond Mean Field

Ugo Mire ^{1,*} and Bernd-Jochen Schaefer ^{1,2,†}

¹*Institut für Theoretische Physik, Justus-Liebig-Universität Gießen, 35392 Gießen, Germany*

²*Helmholtz Forschungsakademie Hessen für FAIR (HFHF), GSI Helmholtzzentrum für Schwerionenforschung, Campus Gießen, 35392 Gießen, Germany*

A comprehensive study of the phase structure of the two-flavor quark–meson–diquark model is presented within the nonperturbative functional renormalization group framework. The influence of mesonic fluctuations beyond the mean-field approximation is investigated, and two-point functions of the diquark fields are computed at finite real-time frequencies. Renormalization group consistency of the effective potential is ensured in order to avoid cutoff artifacts. Substantial modifications of the phase structure are found once mesonic fluctuations are included, and for sufficiently strong diquark couplings the dynamics become dominated by diquark condensation. These effects are elucidated through an analysis of the diquark pole mass and the Silver-Blaze property.

I. INTRODUCTION

The microscopic theory governing strong-interacting matter is quantum chromodynamics (QCD), whose asymptotically free running coupling increases logarithmically with decreasing momentum scale. This scale dependence implies that at low energies the strong coupling becomes large, leading to a rich spectrum of bound states and the dynamical emergence of key non-perturbative phenomena such as spontaneous chiral symmetry breaking and confinement.

While at sufficiently high energy or baryon densities QCD becomes amenable to perturbative methods for weakly-interacting quarks and gluons due to asymptotic freedom, low-energy QCD requires nonperturbative techniques to account for the dynamical changes of the relevant degrees of freedom.

In the low-density and low-temperature region, hadronic effective field theories incorporating chiral symmetry and confinement provide a successful description of equilibrium thermodynamics and the hadronic spectrum, see the review [1]. As baryon density increases, several qualitative changes in the ground state of QCD are expected to occur: chiral symmetry is anticipated to be restored, quark matter may exhibit various color-superconducting phases, and more exotic possibilities such as crystalline or inhomogeneous phases have been proposed [2–13]. Mapping out these regimes and determining the corresponding equation of state (EoS) remains a major challenge, largely because the sign problem prevents lattice QCD from providing first-principles results at finite chemical potential, see, e.g., Refs. [14–17].

At finite baryon density, functional nonperturbative methods such as the functional renormalization group (FRG) and Dyson-Schwinger equations (DSE) constitute the only first-principles approaches capable of directly

accessing QCD thermodynamics. Nevertheless, lattice results on the phase structure and on conserved-charge fluctuations remain indispensable benchmarks for functional QCD methods at $\mu_B = 0$, see the recent review [18]. Functional methods have now reached quantitative control up to the regime $\mu_B/T \lesssim 4.5$, enabling studies of the QCD EoS and phase diagram at moderate densities in a systematic manner; see, e.g., Refs. [13, 19–22].

The FRG framework employed in this work builds upon these advances by using a systematically improvable low-energy truncation that incorporates key insights from first-principles QCD at finite temperature and density [23–28]. A central result of these studies is that the gluonic sector of QCD decouples efficiently at momenta around 1 GeV, owing to the dynamical gluon mass gap. This decoupling justifies the construction of quantitatively reliable low-energy effective descriptions in which the dominant infrared physics is encoded in quark, meson, and diquark degrees of freedom [8]. At even lower energies, most hadronic modes decouple as well, further supporting the success of chiral effective field theories, such as quark–meson models, in describing low-temperature and low-density QCD.

Consequently, low-energy QCD can be accurately captured without explicitly resolving the full gluonic dynamics, provided that the matching to QCD in the ultraviolet is performed consistently and that renormalization-group constraints are respected. This motivates the use of quark–meson–diquark (QMD)–type models [29–33], which have also been introduced in the context of two-color QCD [34–37]. Supplemented by FRG evolution, these models provide controlled low-energy frameworks for investigating thermodynamic properties and the equation of state at finite temperature and density. Such models allow one to incorporate chiral symmetry breaking, diquark pairing, and potential color-superconducting phases while maintaining a close connection to underlying QCD dynamics through their renormalization group (RG) structure.

The FRG provides a particularly suitable framework to investigate this decoupling and the emergence of hadronic

* ugo.louis.tryphon.mire@physik.uni-giessen.de

† bernd-jochen.schaefer@uni-giessen.de

bound states from QCD, see Refs. [38, 39] for early works. Within this approach, composite fields can be incorporated dynamically via dynamical hadronization [40], yielding low-energy effective theories that remain consistently embedded in the underlying quark-gluon dynamics. In practice, this procedure leads to Polyakov-loop-extended Nambu–Jona-Lasinio (NJL)- or quark-meson-type models, with additional diquark channels emerging once quantum, thermal and density fluctuations are taken into account [28, 41, 42]. Recently, related FRG studies have explored quark-diquark models as effective descriptions of baryonic degrees of freedom, including an extrapolation to a QMD model, thereby providing a complementary description of bound-state formation in the low-energy regime of QCD [31, 43].

Motivated by these developments, we employ here an effective low-energy truncation that explicitly includes diquark degrees of freedom and is tailored to intermediate and high quark densities. This construction is guided by recent FRG results on QCD quark-gluon dynamics [44, 45], thereby providing a first step towards a QCD-constrained FRG study of the QMD model at finite temperature and density.

Specifically, we investigate a two-flavor QMD model truncation as a low-energy realisation of the two-flavor color-superconducting (2SC) phase of QCD at moderate baryon density. At asymptotically large densities, the QCD ground state is expected to be in the color-flavor-locked (CFL) phase [3, 4, 12]. At lower chemical potentials, differences in the effective quark masses become more pronounced, leading to mismatched Fermi momenta and disfavoring CFL pairing. This, in turn, modifies the conditions for Cooper pairing among quarks and can change the preferred pairing patterns. In the density regime, where strange quarks effectively decouple, phases such as the 2SC phase, may therefore become favored [3].

Recent FRG analyses revealed that at low densities the dynamics is mostly governed by the (pseudo)scalar

mesonic channel associated with chiral symmetry breaking, while at higher densities attractive diquark correlations become more dominant, cf Refs. [46, 47], in agreement with weak-coupling results at asymptotically large densities [48, 49]. We present a detailed study of the QMD model at finite temperature and density in order to clarify how thermal and density fluctuations influence the competition between chiral and diquark ordering and consequently, the resulting phase structure.

This paper is organized as follows. In Sec. II we briefly introduce the QMD model, with emphasis on some of its symmetry properties. In Sec. III we present our FRG approach for deriving the thermodynamic grand potential, discuss its relation to the often employed mean-field approximation (MFA), and explain how cutoff artifacts are treated via RG consistency (RGC). In Sec. IV we provide details on the computation of the two-point functions of the diquark field in vacuum. Numerical results are summarized in Sec. V. We conclude in Sec. VI with a summary and outlook. Several technical details are collected in Apps. A to C.

II. LOW-ENERGY REALIZATION OF QCD

The two-flavor QMD model is an effective low-energy description of QCD that captures the essential aspects of chiral symmetry breaking and color superconductivity. We begin with a brief analysis of its symmetries, emphasizing the transformation properties of the diquark field under color and flavor rotations.

A. The quark-meson-diquark model

The Euclidean classical action of the $N_f = 2$ flavor and $N_c = 3$ color QMD model at finite temperature $\beta = 1/T$ and quark chemical potential μ reads

$$S[\bar{q}, q, \phi, \Delta, \Delta^*] = \int_0^\beta dx_0 \int d^3x \left\{ \bar{q} \left[\not{\partial} - \mu \gamma_4 + g_\phi (\sigma + i\gamma_5 \vec{\pi} \cdot \vec{\tau}) \right] q + \frac{1}{2} g_\Delta (\Delta_{\mathbf{a}} \bar{q} \gamma_5 \tau_2 i \epsilon_{\mathbf{a}} C \bar{q}^T - \Delta_{\mathbf{a}}^* q^T C \gamma_5 \tau_2 i \epsilon_{\mathbf{a}} q) \right. \\ \left. + \frac{1}{2} (\partial_\mu \phi)(\partial_\mu \phi) + (\partial_\mu + 2\mu \delta_{\mu 4}) \Delta_{\mathbf{a}}^* (\partial_\mu - 2\mu \delta_{\mu 4}) \Delta_{\mathbf{a}} + U(\phi^2, |\Delta|^2) - h\sigma \right\}. \quad (1)$$

It describes the interactions between quark fields, q and \bar{q} , and effective degrees of freedom associated with the σ - and $\vec{\pi}$ -mesons, as well as diquark fields Δ and Δ^* .

The mesonic fields are grouped into the $O(4)$ -symmetric chiral field $\phi = (\sigma, \vec{\pi})$, which provides a convenient basis for the chirally invariant quantity $\phi^2 = \sigma^2 + \vec{\pi}^2$. The potential $U(\phi^2, |\Delta|^2)$ encodes the meson-meson, diquark-meson as well as diquark-diquark interactions consistent with the underlying chiral and color

symmetries. The diquark invariant is given by $|\Delta|^2 = \sum_{\mathbf{a}} \Delta_{\mathbf{a}}^* \Delta_{\mathbf{a}}$, where \mathbf{a} runs over the $N_c = 3$ antisymmetric color generators in the fundamental representation.

In the present work, we restrict ourselves to the minimal truncation

$$U(\phi^2, |\Delta|^2) = \frac{1}{2} m_\phi^2 \phi^2 + \frac{1}{4} \lambda_\phi \phi^4 + m_\Delta^2 |\Delta|^2, \quad (2)$$

which comprises quadratic mass terms for the mesonic

and diquark fields as well as a quartic self-interaction in the mesonic sector. The quark fields q and \bar{q} are Dirac spinors carrying color and flavor indices and transform in the fundamental representation of the color group $SU(3)_c$. The two Yukawa couplings g_ϕ and g_Δ describe the flavor- and color-blind quark-meson and quark-diquark couplings. The explicit chiral symmetry breaking is implemented with a linear term in the radial sigma direction with strength h , generating finite current quark masses and, consequently, non-vanishing pion masses. As a result, the chiral phase transition at vanishing density becomes a smooth crossover rather than a sharp second-order transition.

The charge-conjugated quark spinors $q^C = C\bar{q}^\top$ and $\bar{q}^C = q^\top C$ are defined using the charge-conjugation matrix $C = \gamma_2\gamma_4$ in Euclidean space, where the Dirac matrices γ_μ are Hermitian, $\gamma_\mu^\dagger = \gamma_\mu$, and satisfy the normalization $\{\gamma_\mu, \gamma_\nu\} = 2\delta_{\mu\nu}$. The Pauli matrices $\vec{\tau} = (\tau_1, \tau_2, \tau_3)$ act in flavor space, while the totally antisymmetric tensor $(\epsilon_a)_{bc} = \epsilon_{abc}$ acts in color space.

The composite, complex-valued scalar diquark fields Δ_a and Δ_a^* are treated as components of a vector in color space. These fields carry the quantum numbers of scalar diquarks with $J^P = 0^+$ and are represented as

$$\Delta_a \sim q^\top C \tau_2 i \epsilon_a \gamma_5 q. \quad (3)$$

In the following, Fraktur indices denote color, while flavor indices are suppressed for clarity.

Owing to the nonvanishing baryon charge of the diquark field, its kinetic term exhibits a qualitatively different structure from that of the mesonic sector. The (composite) diquarks carry baryon number $B = 2/3$, and the quark chemical potential couples to baryon number as the temporal component of an external $U(1)_B$ gauge field. Accordingly, the ordinary derivative is promoted to a covariant one

$$\partial_\mu \rightarrow \partial_\mu \mp 2\mu\delta_{\mu 4}, \quad (4)$$

which modifies only the temporal component and incorporates the finite-density background. The opposite signs for Δ_a and Δ_a^* ensure invariance under global $U(1)_B$ transformations and implement the coupling to the conserved charge. In contrast, the mesonic fields carry zero baryon number and therefore do not couple directly to the chemical potential at the kinetic level. The resulting diquark kinetic term thus provides the minimal realization of finite-density effects for charged composite bosons, leading to a μ -dependent dispersion relation.

In the present truncation, we neglect wave-function renormalization effects for all fields, in contrast to Ref. [31], where the diquark wave-function renormalization was argued to play an important role in controlling medium-induced divergences. Here, however, cutoff artifacts are treated by means of RG-consistent flows, as we will discuss in Sec. III D. As demonstrated in Ref. [31], this procedure can be used instead of a standard renormalization scheme, such that the counterterms typically

associated with diquark wave-function renormalization are generated dynamically within the flow.

B. Symmetries of the model

For two quark flavors and in the chiral limit, the QMD model exhibits the global symmetry $SU(3)_c \times SU(2)_L \times SU(2)_R \times U(1)_B$, corresponding to color, chiral flavor, and baryon number conservation¹. The meson fields form a chiral multiplet under $SU(2)_L \times SU(2)_R$, while the scalar diquark fields transform as color antitriplets and carry nonzero baryon charge. In the vacuum, a finite expectation value of the sigma field spontaneously breaks chiral symmetry according to $SU(2)_L \times SU(2)_R \rightarrow SU(2)_V$, generating constituent quark masses and three (pseudo-)Nambu-Goldstone pions.

At sufficiently large baryon chemical potential, the formation of a diquark condensate becomes energetically favored, leading to spontaneous breaking of baryon number symmetry $U(1)_B$. Simultaneously, the global color symmetry is broken according to $SU(3)_c \rightarrow SU(2)_c$, corresponding to the 2SC phase. Due to the global color symmetry breaking, the spontaneous breaking produces $(8-3)$ additional Goldstone modes, leaving one massive radial diquark mode. In a local gauge theory these modes would instead correspond to $(8-3)$ massive gauge bosons via the Anderson-Higgs mechanism. Thus, depending on the model parameters, chiral and diquark condensates may coexist over a range of densities, resulting in simultaneous breaking of chiral, baryon, and color symmetries. The QMD model captures the transition from a chirally broken hadronic phase to a color-superconducting phase driven by diquark condensation.

The chiral (pseudo)scalar interaction sector is a color singlet and therefore preserves the global color symmetry of the model. Conversely, the diquark interaction channel is invariant under chiral $SU(2)_L \times SU(2)_R$ transformations and does not modify the chiral symmetry structure. This separation becomes manifest upon inspecting the transformation properties of the corresponding interaction terms.

The diquark fields and their conjugates are invariant under chiral transformations of the quark fields,

$$q \rightarrow U_\chi q, \quad U_\chi \in SU(2)_L \otimes SU(2)_R \quad (5)$$

and thus transform as chiral singlets. To see this, introduce the chiral projectors

$$P_{L/R} = (1 \mp \gamma_5)/2, \quad U_\chi = U_L P_L + U_R P_R, \quad (6)$$

with

$$q_{L/R} \rightarrow U_{L/R} q_{L/R}, \quad U_{L/R} = \exp\left(i\vec{\theta}_{L/R} \cdot \vec{\tau}\right), \quad (7)$$

¹ The axial $U(1)_A$ symmetry is assumed to be maximally broken by the QCD axial anomaly, as expected from instanton-induced interactions.

then the diquark fields transform as

$$\begin{aligned}\Delta_a &\rightarrow q^\top (U_L^\top P_L + U_R^\top P_R) C \tau_2 i \epsilon_a \gamma_5 (U_L P_L + U_R P_R) q \\ &\rightarrow q^\top C (U_L^\top \tau_2 U_L P_L + U_R^\top \tau_2 U_R P_R) i \epsilon_a \gamma_5 q \\ &\rightarrow q^\top C \tau_2 i \epsilon_a \gamma_5 q = \Delta_a.\end{aligned}\quad (8)$$

Here the relation $\vec{\tau} = -\tau_2 \vec{\tau}^\top \tau_2$, a direct consequence of the pseudo-reality of the Pauli matrices $\vec{\tau}^* = -\tau_2 \vec{\tau} \tau_2$, has been used. Hence, a finite diquark condensate does not break chiral symmetry.

In contrast, the diquark fields transform non-trivially under color transformations as a color anti-triplet. For a color transformation of the quark fields,

$$q \rightarrow Uq, \quad U \in SU(3)_c, \quad (9)$$

the diquark fields transform as

$$\Delta_a \rightarrow q^\top C \tau_2 i (U^\top \epsilon_a U) \gamma_5 q. \quad (10)$$

Using for any $M \in SU(3)$ the identity

$$\epsilon_{abc} M_{ad} M_{be} M_{cf} = \epsilon_{def}, \quad (11)$$

one finds

$$U^\top \epsilon_a U = U_{ab}^* \epsilon_b. \quad (12)$$

Hence, the diquark fields transform according to the color anti-triplet representation,

$$\Delta_a \rightarrow U_{ab}^* \Delta_b, \quad a = 1, 2, 3. \quad (13)$$

Finally, let us comment on the baryon number symmetry. Under a global $U(1)_B$ rotation with angle θ , the diquark field transforms as

$$\Delta_a \rightarrow e^{2/3i\theta} \Delta_a, \quad (14)$$

with baryon charge $B = 2/3$. A finite diquark condensate explicitly breaks the naive baryon number symmetry. However, the condensate locks color and baryon transformations such that a linear combination of the original $U(1)_B$ generator and a generator of the color group remains unbroken. This residual symmetry can be interpreted as a rotated (or shifted) baryon number [50], implying that no independent global symmetry is actually broken and thus no additional Goldstone mode arises.

III. FUNCTIONAL RENORMALIZATION GROUP

The FRG is a powerful method which allows one to incorporate both bosonic and fermionic fluctuations in a nonperturbative manner. In the past, the Euclidean formulation of the FRG has been applied successfully to

investigate the phase structure of quark-meson models and variants thereof [36, 37, 51–58].

For our analysis at moderate and high densities including low temperatures we employ a standard 1PI flow pioneered by Wetterich [59]. It is a functional differential equation for the quantum average effective action Γ_k which depends on the infrared RG cutoff scale k

$$\partial_t \Gamma_k[\Phi] = \frac{1}{2} \text{STr} \left[\left(\Gamma_k^{(2)}[\Phi] + R_k \right)^{-1} \partial_t R_k \right], \quad (15)$$

and has a simple one-loop structure in terms of the full field- and momentum-dependent propagator. The infrared cutoff is introduced through the regulator function R_k , which represents an infrared (IR) mass term that vanishes in the IR as $k \rightarrow 0$, see App. A for details. Quantum fluctuations below the cutoff scale $p^2 \lesssim k^2$ are suppressed and are integrated out by lowering the scale k . The logarithmic scale derivative $t = \ln k/\Lambda$ implements the so-called RG-time with the reference scale to be the ultraviolet (UV) cutoff scale of the flow Λ and runs from 0 to $-\infty$. The physical theory is obtained in the infrared limit $k \rightarrow 0$ with the physical effective action $\Gamma[\Phi] \equiv \Gamma_{k=0}[\Phi]$.

The superfield Φ collects all fundamental fields of the theory, and accordingly, the regulator function R_k is understood as a matrix in this field space. The supertrace STr comprises momentum integrations and sums over all internal indices, such as Lorentz indices and field species, including the appropriate minus signs for fermionic contributions. The n -point field derivatives of the flow of the average effective action are defined as

$$\Gamma_{\Phi_1 \dots \Phi_n, k}^{(n)}(p_1, \dots, p_{n-1}) = \int_{p_n} \frac{\delta^n \Gamma_k[\Phi]}{\delta \Phi_1(p_1) \dots \delta \Phi_n(p_n)}, \quad (16)$$

which leads to an infinite coupled tower of flows of its n -th moments. The momentum integration $\int_{p_n} \equiv \int \frac{d^4 p_n}{(2\pi)^4}$ eliminates the overall factor $(2\pi)^4 \delta(p_1 + \dots + p_n)$, which enforces momentum conservation at each vertex. Consequently, the momentum $p_n = -(p_1 + \dots + p_{n-1})$ is implicitly understood on the left-hand side of Eq. (16).

Numerical or analytical solutions of the flow equation require a systematic truncation scheme for the effective action. A widely used scheme is the derivative expansion, in which all correlation functions are retained while their momentum dependence is expanded in powers of external momenta. At leading order, corresponding to the zeroth-order derivative expansion also known as local-potential approximation (LPA), only point-like interactions without momentum dependence are included. These contributions are encoded in a scale-dependent effective potential that resums local interactions to all orders in the fields.

A. Quark-meson flows with diquarks

As the initial condition for the Wetterich flow Eq. (15) at $k = \Lambda$, we take the QMD Lagrangian introduced above. At leading order of the derivative expansion, i.e., in LPA, the effective action at finite quark chemical potential μ and inverse temperature $\beta = 1/T$ reads

$$\begin{aligned} \Gamma_{k=\Lambda}[\Phi] = & \int_0^\beta dx_0 \int d^3x \left\{ \bar{q} [\not{\partial} - \mu\gamma_4 + g_\phi (\sigma + i\gamma_5 \vec{\pi} \cdot \vec{\tau})] q \right. \\ & + \frac{1}{2} g_\Delta (\Delta_\alpha \bar{q} \gamma_5 \tau_2 i \epsilon_\alpha C \bar{q}^\top - \Delta_\alpha^* q^\top C \gamma_5 \tau_2 i \epsilon_\alpha q) \\ & \left. + \frac{1}{2} (\partial_\mu \phi)^2 + U_k(\phi^2, |\Delta|^2) - h\sigma \right\}, \end{aligned} \quad (17)$$

with the superfield

$$\Phi = (q, \bar{q}, \phi, \Delta, \Delta^*). \quad (18)$$

The quarks \bar{q} and q carry two flavor degrees of freedom and are coupled via g_ϕ to the chiral scalar σ field and to the pseudoscalar pion fields $\vec{\pi}$. At lower energy scales, emergent bound-state degrees of freedom are accounted for through a scale-dependent effective potential $U_k(\phi^2, |\Delta|^2)$ that resums mesonic and diquark (self-)interactions to all orders in the fields. The scale dependence is encoded solely in the effective potential $U_k(\phi^2, |\Delta|^2)$.

The omission of a diquark kinetic term in Eq. (17) corresponds to neglecting the diquark fluctuations and can be justified in the symmetry-broken phase. In a first-principles treatment, the formation of a diquark condensate induces gluonic masses via the Higgs mechanism. The corresponding would-be Goldstone modes associated with the diquark condensate are generally gauge dependent but are completely removed from the spectrum in unitary gauge. If, in addition, both the massive gluons and the radial (non-Goldstone) diquark mode are assumed to be heavy, they decouple from the low-energy dynamics and the remaining description effectively reduces to a mean-field treatment of the diquark sector. This reasoning, however, does not extend to the symmetric phase, where diquark fluctuations are expected to become dynamically relevant, especially in the vicinity of a phase transition.

Under this assumption, the flow of the effective potential is obtained by evaluating the Wetterich equation Eq. (15) on homogeneous constant background fields. Exploiting the global symmetries of the model (see Sec. IIB), the chiral field can be oriented without loss of generality in the σ -direction,

$$\phi(x) = (\sigma, 0, 0, 0) \quad \text{with} \quad \sigma \in \mathbb{R}, \quad (19)$$

excluding a vacuum expectation value for the pseudoscalar isotriplet components.

Similarly, the diquark field can be rotated into a fixed color direction, which we choose as

$$\Delta_\alpha(x) = \Delta \delta_{\alpha 3} \quad \text{with} \quad \Delta \in \mathbb{R}. \quad (20)$$

Due to the $SU(3)_c$ symmetry, only the modulus of the complex-valued diquark condensate, $|\Delta| = \sqrt{\Delta^* \Delta}$, is physically relevant, while its orientation in color space is arbitrary.

The derivation of the flow, Eq. (15), requires the regularized propagators of quarks, diquarks and mesons in this background. The bosonic contribution from the chiral sector follows standard lines and can be found in the literature, see e.g. Ref. [52]. The fermionic contribution is more involved due to the Yukawa coupling between quarks and composite diquarks, which induces a non-trivial mixing structure in the quark propagator.

The inverse regularized quark propagator is a (2×2) -matrix in the field space $\Psi = (q, \bar{q})$

$$G_{q,k}^{-1}(p) = \Gamma_{\Psi^\top \Psi, k}^{(2)}(p) + R_k(p). \quad (21)$$

In the infrared limit $k \rightarrow 0$, the regularized propagator becomes the full quark propagator $G_{q,k=0}$, which is related to the connected two-point correlation functions via

$$\begin{aligned} \begin{pmatrix} \langle q^\top(-p)q(l) \rangle & \langle \bar{q}(-p)q(l) \rangle \\ \langle q^\top(-p)\bar{q}^\top(l) \rangle & \langle \bar{q}(-p)\bar{q}^\top(l) \rangle \end{pmatrix} = \\ G_{q,k=0}(p) \times (2\pi)^4 \delta^{(4)}(p+l), \end{aligned} \quad (22)$$

where we use a Fourier convention in which both q and \bar{q} are assigned incoming momenta.

The four-dimensional Dirac δ -function ensures translational invariance, and $\langle \dots \rangle$ denote connected correlators. In the present representation, the off-diagonal components describe normal quark and antiquark propagation, whereas the diagonal entries correspond to anomalous propagators familiar from Bardeen–Cooper–Schrieffer (BCS) theory. This assignment is opposite to the conventional Nambu–Gor’kov basis, in which the anomalous contributions reside in the off-diagonal elements [60, 61].

The regulator function $R_k(p)$ depends only on spatial momentum \vec{p}

$$R_{q,k}(p) = \begin{pmatrix} 0 & i\vec{p}^\top r_q(x) \\ i\vec{p} r_q(x) & 0 \end{pmatrix}, \quad (23)$$

where $\vec{p} = p_i \gamma_i$ and $r_q(x)$ is a dimensionless shape function of the momentum ratio $x = \vec{p}^2/k^2$. In combination with the kinetic quark term in $\Gamma_{\Psi^\top \Psi, k}^{(2)}$, this choice amounts to a multiplicative modification of the spatial momentum, hereafter denoted the regularized momentum $\vec{p}_{\text{reg},q} = \vec{p}(1+r_q(x))$. An analogous construction applies in the bosonic sector, yielding $\vec{p}_{\text{reg},b}^2 = \vec{p}^2(1+r_b(x))$; see App. A for details.

The explicit inversion of the quark propagator $G_{q,k}^{-1}$ in Eq. (21), including its non-trivial color structure, is deferred to App. B. There, we show that the resulting propagator naturally decomposes into two sectors, which can be expressed in terms of the color-space projectors

$$P_r = \text{diag}(1, 1, 0), \quad \text{and} \quad P_b = \text{diag}(0, 0, 1), \quad (24)$$

corresponding to the paired red-green and the spectator blue sector, respectively. The full propagator then reads

$$G_{q,k}(p) = \begin{pmatrix} \Xi^\dagger(p) & G_\Delta(p) \\ \bar{G}_\Delta^\dagger(p) & \Xi(p) \end{pmatrix} P_{rg} + \begin{pmatrix} 0 & G_0(p) \\ \bar{G}_0^\dagger(p) & 0 \end{pmatrix} P_b. \quad (25)$$

In the following, for notational simplicity, we denote the regularized momenta $\vec{p}_{\text{reg},q}$ by p in all propagators and energy projectors.

One immediately recognizes that consistently with the symmetry-breaking pattern $SU(3)_c \rightarrow SU(2)_c$, the two quark colors in the red-green sector remain degenerate, while the blue quark propagates as an unpaired spectator mode.

At finite temperature, we employ the standard imaginary-time (Matsubara) formalism, in which the Euclidean time direction is compactified and as a consequence, the temporal momentum component becomes discrete [62]. For antisymmetric fields the components are replaced by fermionic Matsubara frequencies $\nu_n = (2n+1)\pi T$.

In the blue sector, at finite temperature and chemical potential, the propagator matrix elements decompose into contributions associated with positive- and negative-energy modes and take the form

$$G_0(p) = \frac{1}{i\nu_n - \epsilon_q^-} P_+ \gamma_4 + \frac{1}{i\nu_n + \epsilon_q^+} P_- \gamma_4. \quad (26)$$

The operators P_\pm and \bar{P}_\pm denote the Dirac energy projectors and are defined in Eqs. (B5) and (B6), respectively. The charge-conjugate propagator satisfies

$$\bar{G}_0(p) = -G_0(-p). \quad (27)$$

This representation of the propagator makes the pole structure manifest and directly yields the finite-density dispersion relations

$$\epsilon_q^\pm = \epsilon_q \pm \mu \quad \text{with} \quad \epsilon_q(\vec{p}) = \sqrt{\vec{p}^2 + m_q^2}. \quad (28)$$

The quark mass $m_q = g_\phi \sigma$ is dynamically generated by the sigma field σ .

In the red-green sector, the propagator matrix elements take a more involved form. They read

$$G_\Delta(p) = \frac{i\nu_n + \epsilon_q^-}{(i\nu_n)^2 - E_q^{-2}} P_+ \gamma_4 + \frac{i\nu_n - \epsilon_q^+}{(i\nu_n)^2 - E_q^{+2}} P_- \gamma_4, \quad (29)$$

with anomalous propagators

$$\Xi(p) = -\Delta_{\text{gap}} \tau_2 i \epsilon_3 C \gamma_5 \left(\frac{\bar{P}_+}{(i\nu_n)^2 - E_q^{+2}} + \frac{\bar{P}_-}{(i\nu_n)^2 - E_q^{-2}} \right), \quad (30)$$

and correspondingly for $\Xi^\dagger(p)$. The charge-conjugate propagator \bar{G}_Δ is related to G_Δ analogously to the blue sector and satisfies

$$\bar{G}_\Delta(p) = -G_\Delta(-p). \quad (31)$$

The quasiparticle dispersion relations are given by

$$E_q^\pm = \sqrt{\epsilon_q^{\pm 2} + \Delta_{\text{gap}}^2} \quad \text{with} \quad \Delta_{\text{gap}} = g_\Delta \Delta. \quad (32)$$

These relations show that, in the presence of a finite diquark condensate, the red and green quarks acquire a gap at the Fermi-surface, characteristic of a superconducting phase. The off-diagonal propagators $G_\Delta(p)$ and $\bar{G}_\Delta^\dagger(p)$ describe the propagation of gapped red and green quarks. By contrast, the diagonal components $\Xi(p)$ and $\Xi^\dagger(p)$ are non-vanishing only for a finite diquark condensate and are directly associated with the spontaneous breaking of the $U(1)_B$ symmetry.

With the full propagator at hand, the Wetterich equation can be employed to derive the flow of the effective potential U_k . Performing the trace over color, flavor, and Dirac indices and evaluating the Matsubara sums yields the general flow equation²

$$\begin{aligned} \partial_t U_k(\sigma, \Delta) = & \frac{1}{4} \int_{\vec{p}} \vec{p}^2 (\partial_t r_b) \left\{ \frac{3}{\epsilon_\pi} \coth \frac{\epsilon_\pi}{2T} + \frac{1}{\epsilon_\sigma} \coth \frac{\epsilon_\sigma}{2T} \right. \\ & - \frac{2N_f}{\epsilon_q} \left[\tanh \left(\frac{\epsilon_q^+}{2T} \right) + \tanh \left(\frac{\epsilon_q^-}{2T} \right) \right. \\ & \left. \left. + 2 \frac{\epsilon_q^+}{E_q^+} \tanh \left(\frac{E_q^+}{2T} \right) + 2 \frac{\epsilon_q^-}{E_q^-} \tanh \left(\frac{E_q^-}{2T} \right) \right] \right\}, \quad (33) \end{aligned}$$

where unified regulator shape functions have been employed, see Eq. (A5).

Using the shorthand notation for derivatives with respect to the squared fields

$$U_k^{(n,m)}(\sigma, \Delta) = \frac{\partial^{n+m} U_k(\sigma, \Delta)}{\partial(\sigma^2)^n \partial(\Delta^2)^m}. \quad (34)$$

the (pseudo)-scalar dispersion relations can be expressed as

$$\epsilon_i = \sqrt{\vec{p}_{\text{reg},b}^2 + m_i^2}, \quad i = \sigma, \pi, \quad (35)$$

with meson masses

$$m_\pi^2 = 2U_k^{(1,0)}(\sigma, \Delta), \quad (36)$$

$$\text{and } m_\sigma^2 = 2U_k^{(1,0)}(\sigma, \Delta) + 4\sigma^2 U_k^{(2,0)}(\sigma, \Delta), \quad (37)$$

which depend on the diquark gap Δ only through the effective potential.

Using a flat regulator (App. A) and replacing the regularized momenta by the RG scale k , $\vec{p}_{\text{reg},b/q}^2 \rightarrow k^2$, the

² For brevity, temperature and chemical potential arguments are omitted hereafter.

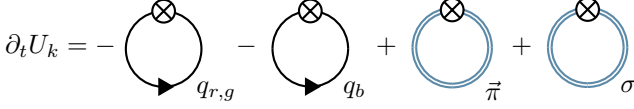


Figure 1. Diagrammatic flow of the quark-meson-diquark model in mLPA. Solid lines denote dressed quark propagators for the red and green quarks $q_{r,g}$ (participating in the superconducting phase) and the blue quark q_b (non-participating). Double solid lines indicate the dressed σ and $\bar{\pi}$ propagators. Crosses mark regulator insertions.

flow equation for the effective potential reads

$$\partial_t U_k(\sigma, \Delta) = \frac{k^5}{12\pi^2} \left\{ \frac{3}{\epsilon_\pi} \coth \frac{\epsilon_\pi}{2T} + \frac{1}{\epsilon_\sigma} \coth \frac{\epsilon_\sigma}{2T} - \frac{2N_f}{\epsilon_q} \left[\tanh \frac{\epsilon_q^+}{2T} + \tanh \frac{\epsilon_q^-}{2T} + 2 \frac{\epsilon_q^+}{E_q^+} \tanh \frac{E_q^+}{2T} + 2 \frac{\epsilon_q^-}{E_q^-} \tanh \frac{E_q^-}{2T} \right] \right\}. \quad (38)$$

This flow receives contributions from four distinct threshold functions, which can be represented as loops with regulator insertions (crosses), as illustrated in Fig. 1. The doubled lines correspond to the σ and $\bar{\pi}$ meson loops, (first line of Eq. (38)), while the second line with quark and antiquark contributions accounts for the unpaired ("blue") quark loop with fermion sign, labeled q_b in the figure. Finally, the coupled red-green quark loop, $q_{r,g}$, carries the diquark gap Δ .

In the following, we refer to this as the *mesonic* local-potential approximation (mLPA), to distinguish it from the full LPA including diquark fluctuations. The thermodynamic (grand) potential is then given by the infrared solution of the flow equation:

$$\Omega(\sigma, \Delta) = U_{k=0}(\sigma, \Delta) - h\sigma. \quad (39)$$

For a given temperature T and chemical potential μ , the thermodynamic phases are determined by the gap equations (the equation of motion)

$$\frac{\partial \Omega(\sigma, \Delta)}{\partial \sigma} \Big|_{\bar{\sigma}, \bar{\Delta}} = \frac{\partial \Omega(\sigma, \Delta)}{\partial \Delta} \Big|_{\bar{\sigma}, \bar{\Delta}} = 0, \quad (40)$$

which minimize the grand potential at the spacetime-independent condensates $\bar{\sigma}$ and $\bar{\Delta}$. Generally, thermodynamic quantities evaluated on the equation of motion are denoted by a bar, as for the physical quark mass \bar{m}_q and physical diquark gap $\bar{\Delta}_{\text{gap}}$.

All thermodynamic quantities follow from standard derivatives of $\Omega(\sigma, \Delta)$, e.g., the entropy density is

$$s = - \frac{\partial \Omega(\bar{\sigma}, \bar{\Delta})}{\partial T}. \quad (41)$$

It is instructive to consider certain limits of the flow equation to gain insight into its structure.

1. Zero temperature flows

At zero temperature and finite chemical potential, the flow Eq. (38) simplifies to

$$\partial_t U_k(\sigma, \Delta) = \frac{k^5}{12\pi^2} \left\{ \frac{3}{\epsilon_\pi} + \frac{1}{\epsilon_\sigma} - \frac{4N_f}{\epsilon_q} \left[\theta(\epsilon_q^-) + \frac{\epsilon_q^+}{E_q^+} + \frac{\epsilon_q^-}{E_q^-} \right] \right\}. \quad (42)$$

For $\Delta = 0$, the fermionic energy ratios reduce to

$$\frac{\epsilon_q^+}{E_q^+} \rightarrow 1 \quad \text{and} \quad \frac{\epsilon_q^-}{E_q^-} \rightarrow 2\theta(\epsilon_q^-) - 1, \quad (43)$$

so that the fermionic flow $N_c \theta(\epsilon_q^-)$ exhibits the Silver-Blaze property at $T = 0$: fermions and antifermions contribute only when $\epsilon_q^- > 0$, i.e., for $\epsilon_q > \mu$, see Sec. IV A.

2. Quark-meson flows

For $\Delta = 0$ and finite temperature, the quasi-particle energies reduce to

$$E_q^+ \rightarrow \epsilon_q^+ \quad \text{and} \quad E_q^- \rightarrow |\epsilon_q^-|. \quad (44)$$

Consequently, the flow converges to that of a quark-meson flow with $N_c = 3$ degenerate colors:

$$\partial_t U_k(\sigma, \Delta = 0) = \frac{k^5}{12\pi^2} \left\{ - \frac{2N_f N_c}{\epsilon_q} \left[\tanh \frac{\epsilon_q^+}{2T} + \tanh \frac{\epsilon_q^-}{2T} \right] + \frac{3}{\epsilon_\pi} \coth \frac{\epsilon_\pi}{2T} + \frac{1}{\epsilon_\sigma} \coth \frac{\epsilon_\sigma}{2T} \right\}. \quad (45)$$

B. Parameter fixing

To solve the flow equation Eq. (38) numerically, the required parameters are fixed from vacuum physics. While the σ -field acquires a non-vanishing vacuum expectation value due to the spontaneous chiral symmetry breaking, the diquark fields are expected to develop nonzero mean values only in dense matter. Accordingly, all couplings and masses in the scalar-pseudoscalar interaction channel of Eq. (38) can be fixed in the standard way from vacuum observables, in contrast to the diquark sector. We adopt $k = \Lambda = 600 \text{ MeV}^3$ as a typical UV scale, in line with recent QCD-motivated low-energy model calculations see e.g. Refs. [41, 63].

³ Later, in the context of RGC, see Sec. III D, we denote this UV scale at which the initial conditions for the effective action are specified by Λ' .

The two parameters a_1 and a_2 of the UV potential, cf. Eq. (2),

$$U_{k=\Lambda'}(\sigma, \Delta) = a_1 \sigma^2 + a_2 \sigma^4 + b_1 \Delta^2, \quad (46)$$

are fixed to the chiral condensate $\bar{\sigma} = f_\pi = 92.4$ MeV and the IR sigma mass $m_\sigma = 560$ MeV in the vacuum⁴. The scalar-pseudoscalar Yukawa coupling is set to $g_\phi = 3.25$ which corresponds to a vacuum quark mass $m_q = 300$ MeV. Finally, we adjust the explicit chiral symmetry breaking parameter h such that the IR pion mass $m_\pi = 137$ MeV is reproduced.

The medium contribution proportional to $\mu^2 \Delta^2$, originating from the diquark kinetic term in the classical action Eq. (1), can be neglected at the UV scale. This corresponds to a vanishing diquark wave-function renormalization at that scale, consistent with the interpretation of the diquark as a composite field introduced via a Hubbard-Stratonovich transformation without an associated kinetic term.

The remaining diquark Yukawa coupling g_Δ is treated as a free parameter. Rather than performing an extensive parameter scan, we choose a few representative values to illustrate the generic physical behavior. The squared diquark mass parameter b_1 is fixed at the UV scale such that the resulting infrared curvature mass,

$$m_{\Delta, \text{curv}}^2 \equiv \Omega^{(0,1)}(\sigma, \Delta)|_{\text{gap}}, \quad (47)$$

evaluated on the equation of motion, Eq. (40), is of the order of the expected physical scale. Consistent with the MFA and mLPA approximations, we neglect the diquark wave-function renormalization in the definition of the curvature mass. We return to this approximation at the end of Sec. V B. Corresponding estimates for the diquark pole mass are given in Refs. [64–66]. Specifically, we set the curvature mass to twice the constituent quark mass, $m_{\Delta, \text{curv}} = 600$ MeV. This choice is motivated by the assumption that, in vacuum, the diquark curvature mass approximately coincides with the corresponding pole mass, although this relation is not guaranteed to hold; see Sec. V B. A detailed analysis of the relation between diquark pole and curvature masses in vacuum QCD will be presented elsewhere [67]. Since the present work focuses on qualitative features of the phase structure, the results are insensitive to the precise parameter values. A summary of all parameters is given in App. C.

C. Recovering mean-field flows

It is instructive to consider the mean-field approximation as a reference limit, which allows us to isolate

and quantify the impact of bosonic fluctuation effects included in the functional approach. In the MFA, quantum and thermal fluctuations of the bosonic fields are neglected in the path integral representation of the grand potential. The mesonic quantum fields are replaced by their classical expectation values, and only the fermionic (quark) determinant is retained, corresponding to the integration over the quark loop. The standard MFA can also be recovered directly from our quark-meson flow equation including diquarks, Eq. (38), by neglecting the bosonic contributions. For an arbitrary regulator, this corresponds to discarding the pion and sigma terms in Eq. (33). This MFA flow can be rewritten in the compact form

$$\partial_t U_k^{\text{MFA}}(\sigma, \Delta) = \partial_t f_k(\sigma, \Delta), \quad (48)$$

with the auxiliary function

$$\begin{aligned} f_k(\sigma, \Delta) = & -2N_f \int_{\vec{p}} \left\{ \frac{1}{2} (|\epsilon_q^-| + 2E_q^-) + \frac{1}{2} (|\epsilon_q^+| + 2E_q^+) \right. \\ & + T \ln \left(1 + e^{-\beta|\epsilon_q^-|} \right) + 2T \ln \left(1 + e^{-\beta E_q^-} \right) \\ & \left. + T \ln \left(1 + e^{-\beta|\epsilon_q^+|} \right) + 2T \ln \left(1 + e^{-\beta E_q^+} \right) \right\}. \end{aligned} \quad (49)$$

Here, we have used the relations

$$\partial_t \epsilon_q = \frac{\vec{p}^2 (\partial_t r_b)}{2\epsilon_q}, \quad \partial_t E_q^\pm = \frac{\epsilon_q^\pm}{E_q^\pm} \partial_t \epsilon_q, \quad (50)$$

in conjunction with Eq. (A5), as well as the identity

$$(\partial_t f) \tanh \frac{f}{2T} = \partial_t [f + 2T \ln(1 + e^{-\beta f})], \quad (51)$$

which holds for an arbitrary function $f(t)$. In Eq. (49) one can clearly see how the contributions from fermions and antifermions combine to account for all three color degrees of freedom.

Since the mean-field flow Eq. (48) is both IR and UV finite, the integration over the RG scale can be carried out analytically

$$\int_{\Lambda}^0 dk \partial_k U_k^{\text{MFA}}(\sigma, \Delta) = f_0(\sigma, \Delta) - f_{\Lambda}(\sigma, \Delta). \quad (52)$$

The grand potential in MFA, Ω^{MFA} , is obtained by supplementing the chirally symmetric effective potential in the infrared $U_{k=0}^{\text{MFA}}$ with the explicit chiral symmetry breaking term

$$\begin{aligned} \Omega^{\text{MFA}}(\sigma, \Delta) &= U_{k=0}^{\text{MFA}} - h\sigma \\ &= U_{\Lambda}^{\text{MFA}}(\sigma, \Delta) - h\sigma \\ &\quad + f_0(\sigma, \Delta) - f_{\Lambda}(\sigma, \Delta). \end{aligned} \quad (53)$$

Due to the finiteness of the flow equation, the function $f_{k=\Lambda}$ effectively controls the divergent momentum integral appearing in $f_{k=0}$. Different choices of shape functions $r_q(x)$ correspond to different regularization schemes

⁴ For numerical convenience, we work at small but finite temperature, $T = 1$ MeV, rather than at strictly zero temperature.

in the standard mean-field formulation. For instance, selecting the sharp shape function

$$(1 + r_q(x))^2 = \frac{1}{\theta(x-1)}, \quad (54)$$

amounts to imposing a conventional three-momentum cutoff $|\vec{p}| = \Lambda$. In this case, the resulting mean-field potential coincides with the standard expressions commonly used in QM-model studies, see, e.g., Ref. [68].

Note that the MFA of the grand potential can also be obtained by standard regularization and renormalization of the UV-divergent⁵ contribution from the one-loop quark determinant to the effective potential, see e.g. Refs. [30, 31, 69]. Performing the MFA within the FRG framework, however, ensures that the same nonperturbative regularization and renormalization schemes are used when comparing with the mLPA results.

D. Renormalization group consistency

In order to remove cutoff artifacts in our low-energy effective theory, we employ the concept of renormalization-group consistency (RGC), see Refs. [29, 70, 71]. Here, we only briefly review the general concept of RGC and its treatment of medium divergences. For a more comprehensive discussion in the context of the QMD model, we refer the reader to Ref. [31]. RGC requires a consistent regularization and renormalization procedure such that the explicit cutoff dependence of the bare action Γ_Λ in the UV compensates the cutoff dependence generated along the flow towards the infrared. As a consequence, the full quantum effective action becomes cutoff independent,

$$\Lambda \frac{d\Gamma}{d\Lambda} = 0. \quad (55)$$

In particular, it has been applied to the computation of the EoS at finite temperature [72] and shown to remove cutoff artifacts in the presence of a diquark condensate [29, 73].

However, in practice, additional external scales of the theory, such as the temperature T or the quark chemical potential μ , can violate this independence, so that the bare action Γ_Λ must vary with changes in these external scales to ensure RGC. In the following, we outline how cutoff artefacts can be consistently removed in our QMD model by enforcing RGC.

The idea is to formally integrate the vacuum flow upward to some higher scale $k = \Lambda > \Lambda'$, assuming that the initial conditions are originally specified by the effective action at a fixed scale Λ'

$$\Gamma_\Lambda[\Phi] = \Gamma_{\Lambda'}[\Phi] + \int_{\Lambda'}^{\Lambda} \frac{dk'}{k'} \mathcal{F}_{k'}[\Phi], \quad (56)$$

with the flow $\partial_t \Gamma_k[\Phi] = \mathcal{F}_k[\Phi]$. In this way, a modified initial condition for the effective action at the higher scale Λ is obtained which yields the same effective action $\Gamma[\Phi]$ in the limit $k \rightarrow 0$. For any intermediate scale $k \neq \Lambda$, RGC then follows directly:

$$\begin{aligned} \partial_\Lambda \Gamma_k[\Phi] &= \partial_\Lambda \int_{\Lambda'}^{\Lambda} \frac{dk'}{k'} \mathcal{F}_{k'}[\Phi] + \partial_\Lambda \int_{\Lambda}^k \frac{dk'}{k'} \mathcal{F}_{k'}[\Phi] \\ &= \partial_\Lambda \Gamma_\Lambda[\Phi] - \mathcal{F}_\Lambda[\Phi] = 0, \end{aligned} \quad (57)$$

demonstrating that the resulting effective action is independent of the choice of Λ .

1. RG consistency in the mean-field flow

The implementation of RGC at the mean-field level of a QMD model is straightforward. In principle, the corresponding RGC initial condition follows directly from the definition of the scale-dependent mean-field potential in Eq. (48).

However, one important difference is that the initial potential at the UV scale – denoted henceforth by the scale Λ' – contains an explicit UV-divergent term proportional to μ^2 in Eq. (49). This medium divergence grows without bound as $\Lambda \rightarrow \infty$, see also Ref. [31] for details.⁶ To handle this divergence without introducing an explicit diquark wave-function renormalization, we perform a Taylor expansion of the upward flow in powers of μ and add the resulting contributions to the right-hand side of Eq. (56). The first term, linear in μ , vanishes due to the symmetry of the effective potential under $\mu \rightarrow -\mu$, corresponding to particle-antiparticle interchange. The second term in the RGC construction, however, consistently captures the medium divergence.

The μ -dependent RGC-improved mean-field condition at $k = \Lambda$ then reads, reinstating the explicit T and μ dependence,

$$\begin{aligned} U_\Lambda^{\text{MFA}}(\sigma, \Delta; \mu) &= U_{\Lambda'}^{\text{MFA}}(\sigma, \Delta; 0, 0) + \mathcal{F}_{\Lambda' \rightarrow \Lambda}(\sigma, \Delta; 0, 0) \\ &\quad + \frac{\mu^2}{2} \partial_\mu^2 \Big|_{\mu=0} \mathcal{F}_{\Lambda' \rightarrow \Lambda}(\sigma, \Delta; 0, \mu), \end{aligned} \quad (58)$$

with the abbreviation for the integrated mean-field flow, see Eq. (48),

$$\begin{aligned} \mathcal{F}_{k_1 \rightarrow k_2}(\sigma, \Delta; T, \mu) &= \int_{k_1}^{k_2} \frac{dk'}{k'} \partial_t f_{k'}(\sigma, \Delta; T, \mu) \\ &= f_{k_2}(\sigma, \Delta; T, \mu) - f_{k_1}(\sigma, \Delta; T, \mu). \end{aligned} \quad (59)$$

At the higher scale Λ , no temperature-dependent medium divergences arise within the MFA, such that the

⁵ Including diquark degrees of freedom introduce additional μ -dependent divergences.

⁶ Due to the presence of a Landau pole, the limit $\Lambda \rightarrow \infty$ cannot be taken. Accordingly, RGC ensures UV-cutoff independence only below the cutoff scale set by the Landau pole.

mean-field potential U_{Λ}^{MFA} is temperature-independent. This contrasts with the initial potential at the lower scale Λ' , which is obtained by integrating the fermionic flow from $k = \Lambda$ to Λ' :

$$U_{\text{init},\Lambda'}^{\text{MFA}}(\sigma, \Delta; T, \mu) = U_{\Lambda}^{\text{MFA}}(\sigma, \Delta; \mu) + \mathcal{F}_{\Lambda \rightarrow \Lambda'}(\sigma, \Delta; T, \mu). \quad (60)$$

Eventually, the scale-dependent mean-field potential follows by integrating the fermionic flow from $k = \Lambda'$ with the modified initial condition Eq. (60):

$$U_k^{\text{MFA}}(\sigma, \Delta; T, \mu) = U_{\text{init},\Lambda'}^{\text{MFA}}(\sigma, \Delta; \mu) + \mathcal{F}_{\Lambda' \rightarrow k}(\sigma, \Delta; T, \mu). \quad (61)$$

Ref. [31] demonstrated that the subtraction of the medium divergence as in Eq. (58) is not unique. In particular, the RGC scheme employed here (the $\sigma\Delta$ scheme in Ref. [31]) yields larger diquark gaps compared to the other schemes and does not satisfy the BCS relation for large chemical potentials. Nevertheless, the qualitative behavior of the QMD model was found to be largely insensitive to the choice of the RGC scheme, which suffices for the present analysis.

2. RG consistency in the mesonic LPA flow

Implementing RGC within the LPA is in general more subtle than in the MFA. Mathematically, RG flows form a semi-group rather than a group: the coarse-graining from the UV to the IR is irreversible and no inverse transformation exists. While this limitation is less severe in the MFA, enforcing RGC in LPA (or beyond) requires particular care.

Technically, this originates from the diffusive character of the bosonic sector. From a fluid-dynamical perspective, the flow Eq. (38) can be recast as a nonlinear advection-diffusion equation. In this interpretation, the fermionic sector acts as a source term, while the pion contribution induces a nonlinear advective term and the sigma contribution generates diffusion, see Refs. [74, 75] for details. As in standard diffusion processes in fluid dynamics, such equations define an irreversible evolution. Consequently, upward integration cannot be employed to reconstruct RGC initial conditions, since diffusion proceeds independently of the direction in which the flow is integrated.

To proceed, we note that in the UV the flow is dominated by fermionic contributions, while bosonic contributions are strongly suppressed due to the increasing meson masses in the threshold functions. At asymptotically large k , the bosonic contributions vanish and thus become irrelevant in this regime. We therefore can proceed similarly to the mean-field procedure described above and integrate only the fermionic flow upward to obtain the RGC condition, and include the bosonic flow once the parameter-fixing scale Λ' is reached. This procedure has also been proposed in Ref. [29].

Thus, in mLPA the T - and μ -dependent RGC initial condition at the scale $k = \Lambda'$ is given by

$$U_{\text{init},\Lambda'}(\sigma, \Delta; T, \mu) = U_{\Lambda'}(\sigma, \Delta; 0, 0) + \mathcal{F}_{\Lambda' \rightarrow \Lambda}(\sigma, \Delta; 0, 0) + \frac{\mu^2}{2} \partial_{\mu}^2 \Big|_{\mu=0} \mathcal{F}_{\Lambda' \rightarrow \Lambda}(\sigma, \Delta; 0, \mu) + \mathcal{F}_{\Lambda \rightarrow \Lambda'}(\sigma, \Delta; T, \mu), \quad (62)$$

with the integrated mean-field flow $\mathcal{F}_{k_1 \rightarrow k_2}(\sigma, \Delta; T, \mu)$, Eq. (59).

In summary, we integrate the flow upward from Λ' to Λ and perform the expansion in μ including only the fermionic contributions. Subsequently, the flow is integrated back in medium, i.e., at finite T and μ , again retaining only the fermionic contributions from Λ to Λ' . This yields the RGC initial conditions at the scale $k = \Lambda'$, from which the mesonic fluctuations are subsequently included.

IV. DIQUARK TWO-POINT FUNCTION

Before presenting our numerical results, we investigate the diquark two-point function. Its pole structure encodes the existence and masses of diquark excitations, thereby offering direct insight into bound-state formation and the onset of diquark condensation as implied by the Silver-Blaze property.

A. Silver-Blaze property

The Silver-Blaze property [76] imposes non-trivial constraints on the 1PI n -point functions and thereby provides valuable guidance for understanding the phase structure of a theory, in particular at finite density. For a general discussion of the Silver-Blaze property, see Ref. [37, 77]; for its phenomenological and field-theoretical implications, see Ref. [78, 79].

At vanishing temperature, it states that the generating functional (or equivalently the partition function) remains independent of the chemical potential μ below the Silver-Blaze threshold μ_c . For a general 1PI n -point function, cf. Eq. (16), this implies that for $\mu < \mu_c$

$$\Gamma_{\Phi_1 \dots \Phi_n}^{(n)}(p_1, \dots, p_{n-1}; \mu) = \Gamma_{\Phi_1 \dots \Phi_n}^{(n)}(\tilde{p}_1, \dots, \tilde{p}_{n-1}; 0), \quad (63)$$

with shifted momenta

$$\tilde{p}_{\varphi} = (p_0 + iq_{\varphi}\mu, \vec{p}), \quad (64)$$

where $q_{\varphi} \in \mathbb{Z}$ denotes the fermion number (or $q_{\varphi}/3$ the baryon number) of the field φ . The critical chemical potential μ_c is determined by the smallest pole mass and the fermion number q_{φ} of those fields that couple to the chemical potential.

For (anti)diquark fields, the fermion numbers are

$$q_{\Delta} = +2 \quad \text{and} \quad q_{\Delta^*} = -2, \quad (65)$$

since (anti)diquarks consist of two fermions or two antifermions, respectively. Applied to the diquark and anti-diquark two-point functions, the Silver-Blaze property yields

$$\Gamma_{\Delta_a^* \Delta_a}^{(2)}(p; \mu) = \Gamma_{\Delta_a^* \Delta_a}^{(2)}(\tilde{p}; 0), \quad (66)$$

with the shifted momenta $\tilde{p} = (p_0 \pm 2i\mu, \vec{p})$.

This relation can be used to infer the chemical-potential dependence of the (anti)diquark pole masses. In general, the pole mass of a (complex scalar) particle ϕ is defined as the zero of its inverse propagator at vanishing three-momentum, $\vec{p} = 0$,

$$\Gamma_{\phi^* \phi}^{(2)}(p_0 = im_\phi, 0; \mu) = 0. \quad (67)$$

For a diquark with fermion number $q_\Delta = +2$, a pole mass at $\mu = 0$ satisfies $\tilde{p}_0 = im_{\Delta, \text{pole}}$ which translates at finite μ to $p_0 = i(m_{\Delta, \text{pole}} - 2\mu)$. Similarly, for an anti-diquark, a pole mass at negative real-time momenta $\tilde{p}_0 = -im_{\Delta^*, \text{pole}}$ leads to $p_0 = i(m_{\Delta^*, \text{pole}} + 2\mu)$. Hence, the diquark pole mass *decreases* linearly with μ ,

$$m_{\Delta, \text{pole}}(\mu) = m_{\Delta, \text{pole}}(0) - 2\mu, \quad (68)$$

while the anti-diquark pole mass *increases* with μ ,

$$m_{\Delta^*, \text{pole}}(\mu) = m_{\Delta^*, \text{pole}}(0) + 2\mu. \quad (69)$$

As a further consequence of the Silver-Blaze property for n -point functions, one can directly infer the chemical-potential dependence of the diquark curvature mass defined in Eq. (47). The dependence of the curvature mass on the chemical potential, defined through the diquark two-point function at vanishing external momentum, is via Silver-Blaze entirely determined by the frequency dependence of the vacuum diquark two-point function

$$m_{\Delta, \text{curv}}^2(\mu) \equiv \Gamma_{\Delta^* \Delta}^{(2)}(0, 0; \mu) = \Gamma_{\Delta^* \Delta}^{(2)}(2i\mu, 0; 0). \quad (70)$$

Consequently, a vanishing diquark pole mass at the Silver-Blaze threshold $\mu = m_{\Delta, \text{pole}}(0)/2$ implies a vanishing curvature mass and the onset of diquark condensation provided that no first-order transition occurs at lower chemical potentials below the threshold.

A similar conclusion also holds for arbitrary mesonic pole and curvature masses carrying vanishing baryon number. However, both masses remain constant throughout the Silver-Blaze region below the threshold, for example

$$m_{\sigma/\pi, \text{curv}}^2(\mu) = m_{\sigma/\pi, \text{curv}}^2(0), \quad (71)$$

and

$$m_{\sigma/\pi, \text{pole}}^2(\mu) = m_{\sigma/\pi, \text{pole}}^2(0). \quad (72)$$

B. Diquark two-point functions in RPA

We first analyze the two-point functions of the (anti)diquarks at finite real-time frequencies within the random-phase approximation (RPA). In this framework, collective excitations arise from fermionic particle-hole scattering, while fluctuations of the composite bosonic fields are neglected. In the context of the FRG, the RPA two-point functions are obtained by computing the two-point functions within LPA (or mLPA) and neglecting all bosonic contributions. In this sense, the construction is analogous to deriving the MFA from the LPA flow equation for the effective potential, as discussed in Sec. III C. The RPA permits an analytical solution and guarantees a consistent regularization of the two-point functions with the underlying mean-field potential. We then improve upon this approximation by computing the diquark two-point function in mLPA, thereby including mesonic fluctuations.

The flow of the two-point correlation functions for the diquark field in RPA is given by

$$\partial_t \Gamma_{\Delta_a^* \Delta_a, k}^{(2)}(p) = \frac{1}{2} \tilde{\partial}_t \Pi_{\Delta_a^* \Delta_a, k}(p), \quad (73)$$

where no summation over the index \mathbf{a} is implied. The polarization loop reads

$$\begin{aligned} & \Pi_{\Delta_a^* \Delta_a, k}(p) \\ &= \int_l \text{Tr} \left[\Gamma_{\Delta_a^* \Psi \Gamma \Psi}^{(3)} G_{q, k}(l) \Gamma_{\Delta_a \Psi \Gamma \Psi}^{(3)} G_{q, k}(p+l) \right], \end{aligned} \quad (74)$$

where $\Psi = (q, \bar{q})$. No four-point vertex $\Gamma^{(4)}$ appears, since bosonic fluctuations are neglected within the RPA (cf. Fig. 2). The trace runs over bispinor space as well as color, flavor, and Dirac indices. The required three-point vertices are

$$\Gamma_{\Delta_a \Psi \Gamma \Psi}^{(3)} = \begin{pmatrix} g_\Delta C \gamma_5 \tau_2 i \epsilon_a & 0 \\ 0 & 0 \end{pmatrix}, \quad (75)$$

$$\Gamma_{\Delta_a^* \Psi \Gamma \Psi}^{(3)} = \begin{pmatrix} 0 & 0 \\ 0 & -g_\Delta C \gamma_5 \tau_2 i \epsilon_a \end{pmatrix}. \quad (76)$$

The RG-time derivative on the right-hand side of Eq. (73) is defined as

$$\tilde{\partial}_t = \int dx [-2x r'_q(x)] \frac{\delta}{\delta r_q(x)}, \quad (77)$$

and acts only on the shape function $r_q(x)$ with $x = \vec{p}^2/k^2$, cf. App. A. Both RG-scale derivatives ∂_t and $\tilde{\partial}_t$ are equivalent since the shape function is the only scale-dependent quantity within the MFA or the RPA.

The flow Eq. (73) can be integrated from the UV scale Λ' down to k , yielding a regularized expression for the diquark two-point function

$$\begin{aligned} \Gamma_{\Delta_a^* \Delta_a, k}^{(2)}(p) &= \Gamma_{\Delta_a^* \Delta_a, \Lambda'}^{(2)}(p) \\ &+ \frac{1}{2} \Pi_{\Delta_a^* \Delta_a, k}(p) - \frac{1}{2} \Pi_{\Delta_a^* \Delta_a, \Lambda'}(p). \end{aligned} \quad (78)$$

$$\partial_t \Gamma_{\Delta_a^* \Delta_a, k}^{(2)} = -2N_c \left[\text{Diagram 1} \right] - \left[\text{Diagram 2} \right] - 3 \left[\text{Diagram 3} \right]$$

Figure 2. Vacuum flow of the diquark two-point function including bosonic (sigma and pion) fluctuations. The flow of the two-point function in RPA is just the first diagram.

The initial conditions at the UV scale Λ' are chosen consistently in terms of the momentum-independent mean-field potential $U_{k=\Lambda'}$, given in Eq. (46), as

$$\Gamma_{\Delta_a^* \Delta_a, \Lambda'}^{(2)}(p) = b_1. \quad (79)$$

This choice corresponds implicitly to a vanishing diquark wave-function renormalization at the scale $k = \Lambda'$ consistent with a composite field introduced via a Hubbard-Stratonovich transformation without a kinetic term at the UV scale.

C. Analytical continuation

To determine the diquark pole mass, we perform an analytic continuation to real time. At vanishing temperature, however, the identification of the pole mass does not strictly require a full analytic continuation with an $i\epsilon$ prescription. In practice, it is sufficient to evaluate the two-point function at purely imaginary frequencies, $p_0 = -i\omega$, to extract the vacuum pole mass, while the $i\epsilon$ prescription becomes relevant only when accessing real-time properties beyond decay thresholds. In the present case, the analytic continuation is nevertheless straightforward and is employed for convenience.

The analytical continuation of the temporal component of the external momentum in the finite-temperature flow equation for the two-point function, $\Gamma_{\Delta_a^* \Delta_a}^{(2)}(p_0, \vec{p})$, is implemented in two steps. After performing the Matsubara frequency sum in the flow equation, the periodicity of the thermal occupation numbers along the imaginary axis of the complex energy plane is employed⁷

$$n_F(\epsilon + ip_0) \rightarrow n_F(\epsilon), \quad (80)$$

where the external Euclidean Matsubara frequencies are discretized as $p_0 = 2\pi nT$ as they originate from the diquark field. With this prescription, the polarization loop Eq. (74) takes with $\epsilon_q = \sqrt{\bar{l}_{\text{reg}}^2 + m_q^2}$ the simple form

$$\begin{aligned} & \Pi_{\Delta_a^* \Delta_a, k}(p_0, 0) = \\ & 16N_f g_\Delta^2 \int_{\bar{l}} \frac{\epsilon_q^2}{4\epsilon_q^2 - (ip_0)^2} \frac{-1 + 2n_F(\epsilon_q)}{\epsilon_q}, \quad (81) \end{aligned}$$

⁷ In this work, only fermionic distributions are needed.

where we have assumed $\mu = 0$.

In the second step, the discrete external Matsubara frequency is analytically continued to the real energy domain according to $ip_0 \rightarrow \omega + i0^+$, which yields the retarded two-point function for vanishing spatial external momentum components, $\vec{p} = 0$

$$\Gamma_{\Delta_a^* \Delta_a}^{(2), R}(\omega) = -\lim_{\epsilon \rightarrow 0} \Gamma_{\Delta_a^* \Delta_a}^{(2), E}(p_0 = -i(\omega + i\epsilon), 0), \quad (82)$$

where ω is the continuous real frequency. In practice, the limit $\epsilon \rightarrow 0$ is not taken analytically but a small imaginary part, $\epsilon = 10^{-8}$ MeV, is retained. We have explicitly verified that the location of the pole masses and the qualitative features of the spectral function are insensitive to the choice of ϵ for $\epsilon \lesssim 0.1$ MeV, see also Ref. [80].

From the two-point function at finite real-time momenta, the pole mass is immediately accessible, as mentioned in Sec. IV A. The diquark pole mass $m_{\Delta, \text{pole}}$ is given by the root of the real part of the retarded two-point function:

$$\text{Re} \Gamma_{\Delta_a^* \Delta_a}^{(2), R}(\omega = m_{\Delta, \text{pole}}) = 0. \quad (83)$$

D. Diquark correlations beyond RPA

The diquark two-point function can also be computed in LPA. In the absence of a diquark condensate, the flow equation of the two-point function simplifies considerably, which motivates our focus on this case.

In the mLPA, the flow of the diquark two-point function at finite temperature includes bosonic fluctuations and is shown diagrammatically in Fig. 2. It is given by

$$\partial_t \Gamma_{\Delta_a^* \Delta_a, k}^{(2)}(p) = \frac{1}{2} \tilde{\partial}_t \Pi_{\Delta_a^* \Delta_a, k}(p) + \frac{1}{2} \tilde{\partial}_t \mathcal{T}_{\Delta_a^* \Delta_a, k}, \quad (84)$$

where $\mathcal{T}_{\Delta_a^* \Delta_a, k}$ denotes a sum of momentum-independent tadpole diagrams of the form

$$\mathcal{T}_{\Delta_a^* \Delta_a, k} = \sum_{\phi=\sigma, \vec{\pi}} \Gamma_{\Delta_a^* \Delta_a \phi \phi, k}^{(4)} \frac{1}{\beta} \sum_n \int_{\vec{p}} G_{\phi \phi, k}(\omega_n, \vec{p}), \quad (85)$$

with bosonic propagators $G_{\phi \phi, k}$ for $\phi = \{\sigma, \vec{\pi}\}$

$$G_{\phi \phi, k}(\omega_n, \vec{p}) = \frac{1}{\omega_n^2 + \vec{p}_{\text{reg}, b}^2 + m_{\phi, k}^2}. \quad (86)$$

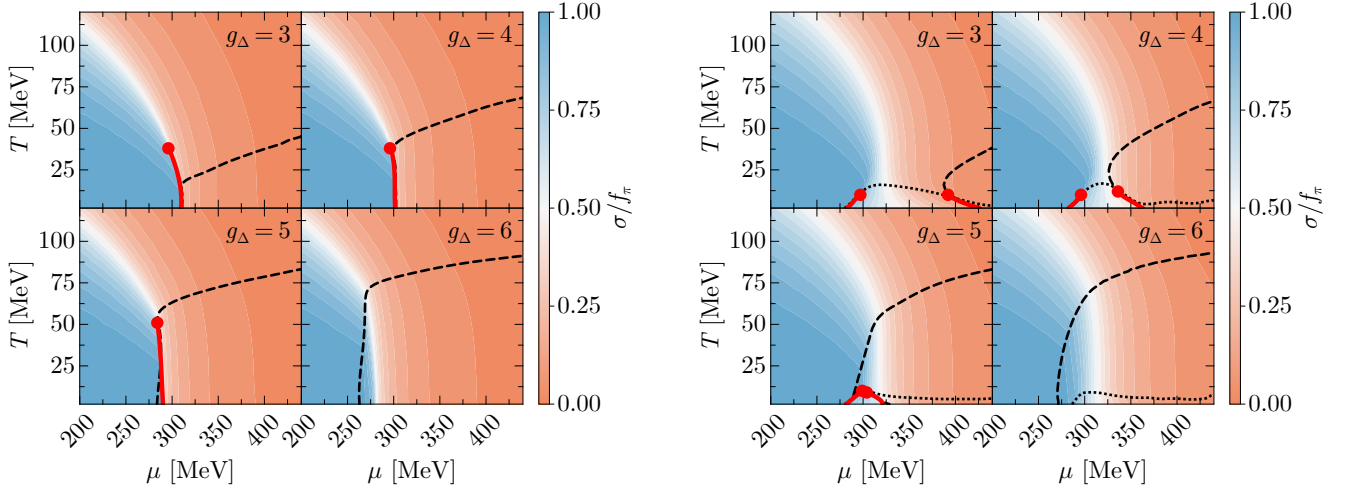


Figure 3. Phase diagrams for the quark-meson-diquark model for different diquark couplings g_Δ in MFA (left) and mLPA (right). The color coding represents the strength of the chiral condensate. Red solid lines indicate first-order chiral phase transitions terminating in a critical endpoint (red dots). In the right panel, dotted lines mark the boundary below which the entropy density becomes negative. The black dashed line denotes the onset of the diquark condensation.

The summation in Eq. (85) runs over three pions and one sigma meson and the scale-dependent four-point vertices $\Gamma_{\Delta_a^* \Delta_a \phi \phi, k}^{(4)}$ are related to derivatives of the meson potential

$$\Gamma_{\Delta_a^* \Delta_a \sigma \sigma, k}^{(4)} = U_k^{(1,1)} + \sigma^2 U_k^{(1,2)}, \quad (87)$$

$$\Gamma_{\Delta_a^* \Delta_a \pi \pi, k}^{(4)} = U_k^{(1,1)}. \quad (88)$$

This identification is valid only in the absence of a diquark condensate. In this case, all three-point vertices of the form $\Gamma_{\Delta_a \phi \phi}^{(3)}$ and $\Gamma_{\Delta_a^* \phi \phi}^{(3)}$ vanish, such that bosonic fluctuations contribute to the diquark two-point flow exclusively via tadpole diagrams.

Performing the $\tilde{\partial}_t$ derivative, Matsubara summation, and momentum integration for the Litim shape function $r_b(x)$ (see App. A), the tadpole contribution reduces to

$$\frac{1}{2} \tilde{\partial}_t \mathcal{T}_{\Delta_a^* \Delta_a, k} = \frac{k^5}{6\pi^2} \sum_{\phi=\sigma, \pi} \frac{\partial m_{\phi, k}^2}{\partial \Delta^2} \times \frac{1}{\epsilon_\phi^2} \left[n'_B(\epsilon_\phi) - \frac{1 + 2n_B(\epsilon_\phi)}{2\epsilon_\phi} \right]. \quad (89)$$

The bosonic dispersion relations are given in Eq. (35) and evaluate to $\epsilon_\phi = \sqrt{k^2 + m_\phi^2}$.

Numerically, an additional flow equation for $\partial_{\Delta^2} U_k$ is solved and used to determine $\partial_{\Delta^2} m_{\phi, k}^2$ for all k . This allows for a direct integration of the flow equation for the diquark two-point function at external momentum $p = (-i(\omega + i\epsilon), \vec{0})$, yielding the retarded two-point function, analogous to the RPA.

V. NUMERICAL RESULTS

We begin by analyzing the phase structure of the QMD model in the mean-field approximation, and compare it to results from the FRG. The impact of diquark pairing on the chiral phase structure is studied by varying the diquark coupling and examining its connection to the pole and curvature masses. Unless explicitly stated otherwise, all results are obtained within the RG-consistent framework.

A. Phase structure

The phase structure of the QMD model in the T - μ plane, obtained in MFA (left) and in mLPA (right) for diquark couplings $g_\Delta = 3 - 6$ is shown in Fig. 3. The chiral phases are indicated in blue (chirally broken) and orange (chirally restored) colors. The chiral crossover appears as a white band, while solid red lines denote the first-order (chiral) transition terminating in a critical endpoint (red dot). The onset of the second-order diquark condensation is indicated by dashed black lines. Additionally, dotted lines in the right FRG results denote the boundary below which the entropy density becomes negative.

In both MFA and mLPA results, the overall topology of the phase diagram remains robust, showing three characteristic regions: (i) a chirally broken and non-superconducting phase at low T and μ , (ii) a chirally restored and superconducting phase at low T and high μ , and (iii) a non-superconducting phase at high T . Quantitatively, the mLPA shifts the chiral transition lines to lower chemical potentials, exhibiting a characteristic back-bending at low temperatures, which reflects the in-

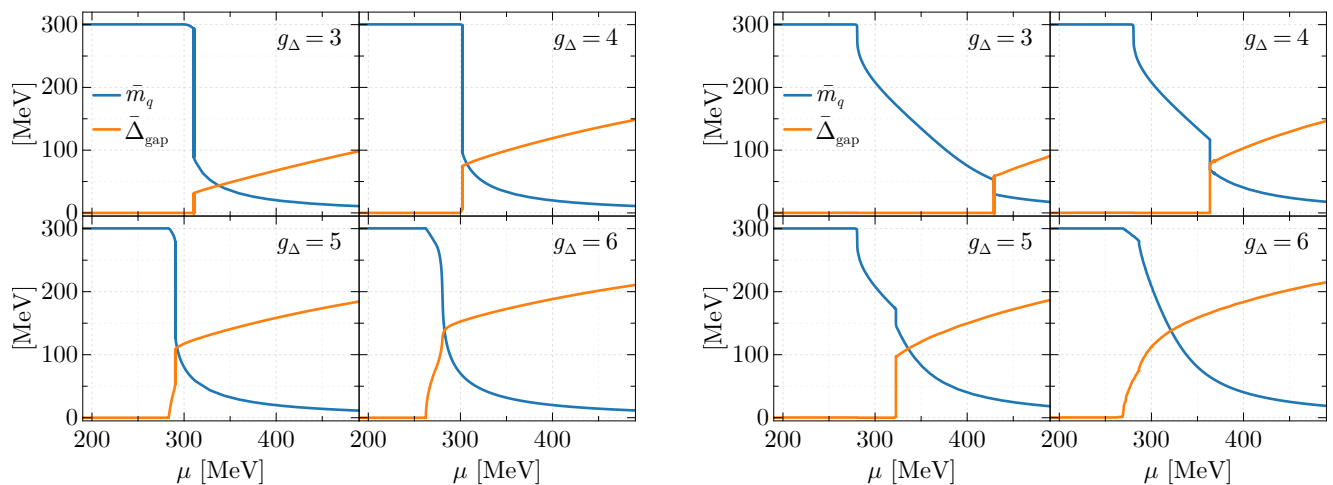


Figure 4. Quark mass $\bar{m}_q = g_\phi \bar{\sigma}$ and the diquark gap $\bar{\Delta}_{\text{gap}} = g_\Delta \bar{\Delta}$ for various diquark couplings g_Δ as functions of the quark chemical potential in MFA (left) and mLPA (right).

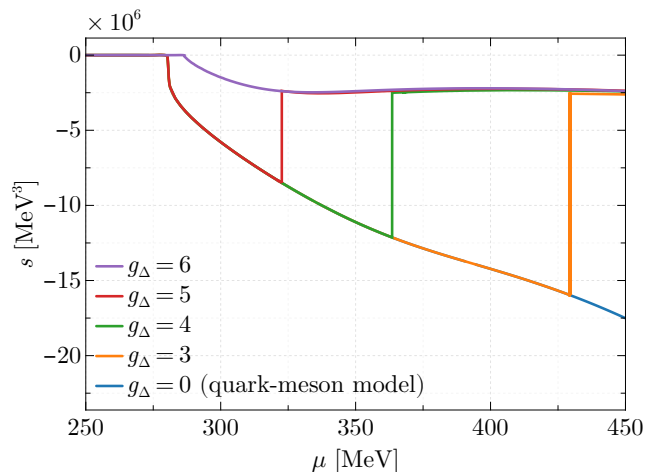


Figure 5. Entropy density s as a function of the chemical potential μ for different diquark couplings g_Δ in the mLPA, compared with a pure quark-meson FRG calculation.

fluence of mesonic and diquark fluctuations. By contrast, in mLPA the onset of diquark condensation is shifted to higher chemical potentials, most prominently at smaller g_Δ , and is accompanied by a forward bending of the condensation line. In addition, a first-order transition terminating at a critical endpoint appears at lower diquark couplings and disappears for larger couplings.

The MFA phase diagrams (Fig. 3, left panels) show that increasing the diquark coupling raises the critical temperature T_c at fixed μ , at which diquark pairing is lost (dashed lines). This is in line with the BCS relation [81],

$$T_c = \frac{e^\gamma}{\pi} \bar{\Delta}_{\text{gap}}(T=0), \quad (90)$$

which links the critical temperature to the zero-temperature diquark gap, see Fig. 4. Despite devia-

tions from the BCS relation at large chemical potentials in the present RGC scheme (see Ref. [31]), the critical temperature remains an increasing function of the zero-temperature diquark gap. Thus, Eq. (90) implies a corresponding rise in T_c with increasing diquark couplings.

This trend persists in the mLPA when mesonic fluctuations are included, but only at higher chemical potentials. Close to the first-order chiral transition, however, mesonic fluctuations significantly modify the phase structure in a manner absent in MFA. Interestingly, for larger diquark couplings ($g_\Delta = 6$ in our case) the first-order transition and its associated endpoint disappear in both MFA and mLPA calculations.

1. Back-bending of the chiral transition line in mLPA

The characteristic back-bending of the chiral transition line at decreasing T (Fig. 3, right panels) has also been observed in other low-energy effective model studies beyond MFA [82–87], as well as in mean-field studies of effective Polyakov-loop theories on the lattice [88]. Due to the Clausius-Clapeyron relation, this back-bending is related to the appearance of a negative entropy density in this region of the phase diagram. In [86], the regulator-scheme dependence of the back-bending was investigated in LPA, revealing a sensitivity to the choice of the shape function. In particular, no negative entropy density was found for momentum-independent Callan-Symanzik-type regulators, in contrast to optimized flat regulators. Since the back-bending is induced at scales around the Fermi surface and appears as a discontinuity in the fermion flow [86], it has been conjectured that a Cooper instability of the Fermi surface driven by attractive pion and sigma exchange may cause the negative entropy [84]. This conjecture can now be tested directly by examining whether the negative-entropy region exhibits

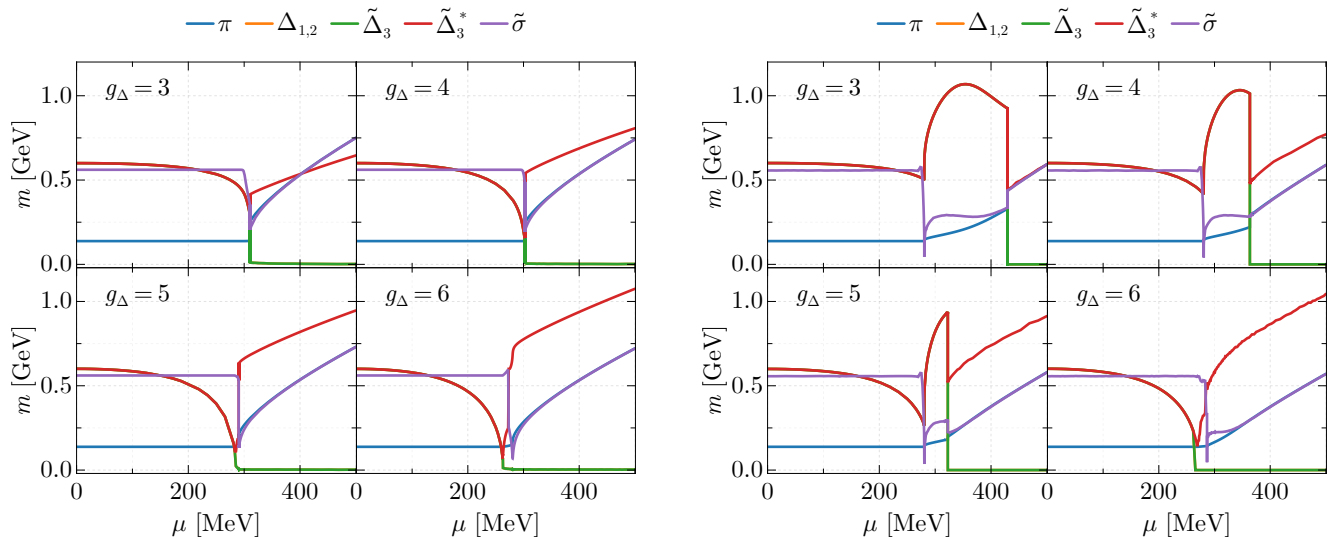


Figure 6. Curvature diquark and meson masses as a function of the quark chemical potential μ for different diquark couplings g_Δ in MFA (left) and mLPA (right). The degeneracy of $\Delta_{1,2}$ and $\tilde{\Delta}_3$ leads to overlapping, indistinguishable curves.

color-superconducting gaps and by assessing the role of diquark condensation in the back-bending.

As can be seen in Fig. 3, the back-bending also affects the diquark onset, which turns into a first-order transition at low temperature and does not intersect the μ -axis perpendicularly. The dotted lines in the figure mark the onset below which the entropy density becomes negative. Increasing the diquark coupling reduces the region of negative entropy, which becomes significantly suppressed for $g_\Delta = 6$. Nevertheless, a finite domain of negative entropy persists even at large chemical potentials μ .

Fig. 5 shows the entropy density s , evaluated in mLPA for different diquark couplings along the chemical potential axis for (almost) vanishing temperature. Below the chiral phase transition in the broken phase ($\mu \lesssim 279$ MeV), s vanishes, consistent with the transition location in the corresponding phase diagram Fig. 3 (right panels). In the chirally restored phase, the entropy density becomes negative, as previously observed in a pure quark-meson model analysis [84] (lower lines with $g_\Delta = 0$ in Fig. 5).

Once diquark condensation sets in, the entropy density is significantly reduced by nearly an order of magnitude and remains approximately constant throughout the 2SC phase. As the diquark coupling increases, the onset of condensation shifts to lower chemical potentials, causing the discontinuities in the entropy associated with the first-order transition to decrease. For $g_\Delta = 6$, these discontinuities disappear altogether.

We conclude that the inclusion of the diquark condensate at the mean-field level mitigates the back-bending of the chiral transition line, leading to a reduced negative entropy density. In particular for $g_\Delta = 6$, this is consistent with Refs. [86, 89], where the back-bending behavior diminishes once the chiral transition changes from

first to second order. Furthermore, the contributions of gapped fermions to thermodynamic quantities with explicit temperature dependence, such as the entropy density, are exponentially suppressed [90]. This suppression may account for the observed improvements, as the back-bending originates from the feedback of bosonic fluctuations on the fermionic flow [86].

An open question is whether this trend persists once diquark fluctuations are included. Clarifying this would help to identify the origin of the observed improvements. At high densities, the thermodynamics is expected to be dominated by the diquark sector, as illustrated in a MFA setting in Ref. [31]. Since the diquark channel is handled at the mean-field level, no negative entropy is expected to arise, leaving it unclear whether the improvement stems from the diquark channel itself or from its mean-field treatment. For comparison, we also examined the impact of the ω -meson on the back-bending and found no significant modification, consistent with Ref. [91].

2. Diquark onset and chiral transition

In MFA, the onset of diquark condensation coincides with the chiral transition at low temperature for $g_\Delta = 3, 4$. For larger couplings ($g_\Delta = 5, 6$), the diquark onset slightly precedes the chiral transition, which changes from first order to a sharp crossover at $g_\Delta = 6$. This behavior can be seen in Fig. 4, where the quark mass and diquark gap are shown as functions of the chemical potential at (almost) vanishing temperatures. A similar pattern is observed in mLPA, at least for sufficiently large diquark couplings. Whenever the diquark onset precedes chiral restoration, it occurs as a second-order transition at $\mu < m_q = 300$ MeV for our parameters. This is con-

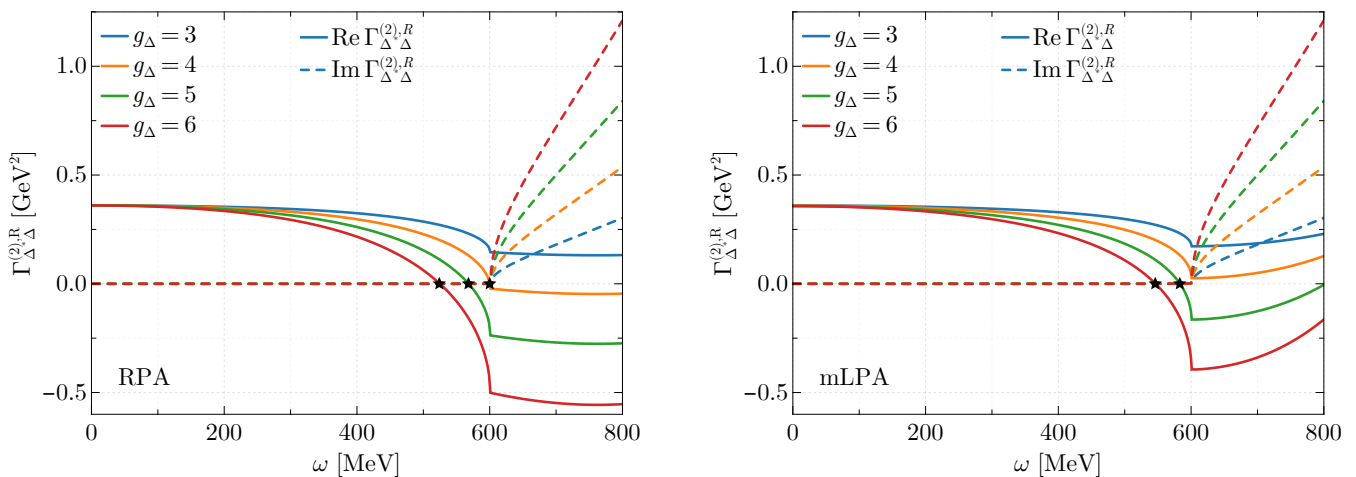


Figure 7. Real (solid lines) and imaginary (dashed lines) parts of the vacuum diquark two-point function as a function of the real-time external frequency ω for various diquark couplings g_{Δ} in RPA (left) and mLPA (right). The black stars mark the locations of the diquark pole masses.

sistent with the Silver-Blaze property, which implies a diquark pole mass smaller than twice the quark mass, $m_{\Delta, \text{pole}} < 600$ MeV, as confirmed below.

B. Pole and curvature masses

In Fig. 6, we show the curvature masses of mesons and diquarks as functions of the chemical potential in MFA and mLPA. At low μ , chiral symmetry breaking yields a heavy sigma meson and three light pions, while the three complex diquark fields remain degenerate in the absence of a diquark condensate. As μ increases within the Silver-Blaze region, $\mu < \mu_c$, the sigma and pion curvature masses remain constant, whereas the diquark curvature mass decreases. Both features are fully consistent with the Silver-Blaze property, see Sec. IV A.

At larger μ , the system enters the chirally restored and color-superconducting phase, where the $U(1)_B$ symmetry is broken. This induces a mixing between the blue diquarks Δ_3, Δ_3^* and the sigma meson, requiring a diagonalization of the mass matrix to obtain the in-medium collective modes, denoted by $\tilde{\Delta}_3, \tilde{\Delta}_3^*$ and $\tilde{\sigma}$. As expected from chiral symmetry restoration, the pion mass becomes degenerate with one of the collective modes, $\tilde{\sigma}$. According to the symmetry-breaking pattern $SU(3)_c \rightarrow SU(2)_c$, we find five Goldstone modes ($\Delta_1, \Delta_1^*, \Delta_2, \Delta_2^*, \tilde{\Delta}_3$) and one massive mode ($\tilde{\Delta}_3^*$), both in MFA and mLPA. The real-time properties of these excitations at finite density will be addressed in a forthcoming publication [92].

In mLPA, however, the back-bending region leaves distinct imprints: at intermediate chemical potentials around the chiral transition, a non-superconducting phase with partial chiral symmetry restoration emerges, characterized by a decreasing sigma mass, an increasing pion mass, and rising (degenerate) diquark masses.

As noted in Sec. V A 2, a second-order onset of diquark condensation at $\mu < m_{q, \text{vac}} = 300$ MeV requires a vacuum diquark pole mass below 600 MeV. This is not reflected in the curvature masses shown in Fig. 6, since our parameter fixing enforces a vacuum diquark curvature mass of 600 MeV (see Sec. III B). To resolve this, we extract the pole mass from the diquark two-point function evaluated at real-time external frequencies, cf. Eq. (83).

In Fig. 7, we show the vacuum diquark retarded two-point function $\Gamma_{\Delta^* \Delta}^{(2),R}(\omega)$ for different diquark couplings in RPA and mLPA, cf. Sec. IV B. At vanishing frequency, the retarded two-point function defines the diquark curvature mass

$$\Gamma_{\Delta^* \Delta}^{(2),R}(\omega = 0) = m_{\Delta, \text{curv}}^2 = (600 \text{ MeV})^2, \quad (91)$$

and hence all computations agree at this point as a consequence of the parameter-fixing procedure, see Sec. III B.

Going to higher external frequencies ω , the real part of the retarded two-point function starts to decrease. For the largest diquark couplings ($g_{\Delta} \geq 4$ in RPA and $g_{\Delta} \geq 5$ in mLPA), the two-point function vanishes already for $\omega < 2m_q = 600$ MeV, corresponding to a finite diquark pole mass. Increasing the diquark coupling results in a decreasing pole mass in both approaches and the imaginary part remains zero up to the threshold at twice the vacuum quark mass, $\omega = 2m_q = 600$ MeV, which marks the onset of the first available decay channel of the diquark field within the present approximation.

We find for $g_{\Delta} > 4$ that the diquark pole mass in Fig. 7 is consistent with twice the onset chemical potential of diquark condensation. In this regime, diquark condensation occurs prior to the chiral transition and is realized as a second-order transition, as shown in Figs. 3 and 4. This behavior is consistent with the Silver-Blaze property (see Sec. IV A), which implies the existence of a diquark pole mass below $2m_{q, \text{vac}} = 600$ MeV as soon as

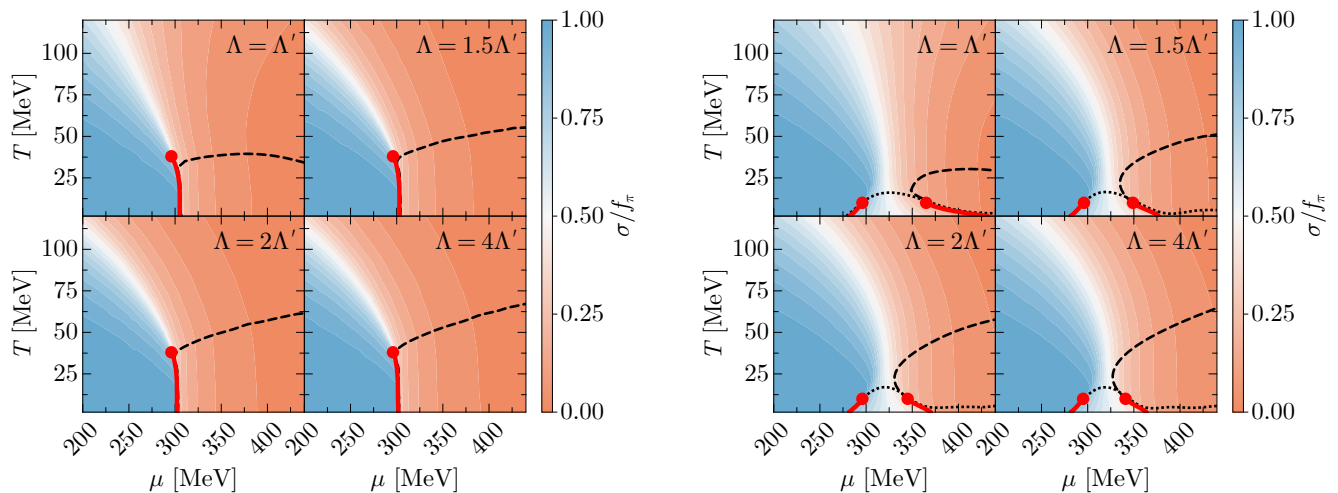


Figure 8. Impact of RG consistency on the phase structure of the quark-meson-diquark model at fixed diquark coupling $g_\Delta = 4$ in MFA (left) and mLPA (right). Color coding and line conventions are as in Fig. 3. With increasing UV scale Λ (at fixed $\Lambda' = 600$ MeV), cutoff artifacts are reduced in both MFA and mLPA, while the back-bending of the transition lines remains unaffected.

the chemical potential of a second-order diquark onset is less than $m_{q,vac}$. In particular, we attribute the reduced back-bending behavior observed in mLPA (cf. Sec. V A 1) for large diquark couplings ($g_\Delta = 6$) to the finite diquark pole mass found in Fig. 7 (right).

Since the diquark curvature mass defined in Eq. (47) is not an RG-invariant quantity, a proper comparison between pole and curvature mass must also account for the diquark wave-function renormalization Z_Δ . The diquark wave-function renormalization and curvature mass are defined through the diquark two-point function as [93]

$$\Gamma_{\Delta^* \Delta}^{(2)}(p) \approx Z_\Delta (m_{\Delta,curv}^2 + p^2) + \mathcal{O}(p^4), \quad (92)$$

which reduces to Eq. (47) for $Z_\Delta = 1$ and $p = 0$. Using our results for the two-point function, cf. Fig. 7, we extract the corresponding values of Z_Δ for different couplings, as summarized in Tab. I.

g_Δ	3	4	5	6
Z_Δ	0.14	0.25	0.39	0.57

Table I. Diquark wave-function renormalization for different diquark couplings. The values obtained in RPA and mLPA differ only by a few percent.

As the diquark coupling decreases, the fermionic contribution to the diquark wave-function renormalization becomes less pronounced, and Z_Δ approaches its bare, initial UV value $Z_{\Delta,k=\Lambda} = 0$, see Eq. (79). This implies that including a wave-function renormalization typically enhances the curvature mass relative to the case without such a correction, provided that Z_Δ is not treated self-consistently in the flow. This suggests that quantitatively relevant corrections may arise from a fully self-consistent

inclusion of the diquark wave-function renormalization, e.g., within an LPA' truncation. Such an extension could improve the agreement between the diquark pole and curvature masses, analogous to the behavior observed for the pion field [93].

C. Consequence of RG consistency

To conclude the discussion of our numerical findings, we assess the impact of RGC on the phase structure. Fig. 8 shows the dependence on the UV cutoff Λ at a fixed diquark coupling $g_\Delta = 4$, in analogy to the previous phase diagrams. In the range $\Lambda = \Lambda'$ to $\Lambda = 1.5\Lambda'$, cutoff artifacts are most pronounced in both transition lines. The chiral transition at lower chemical potentials bends towards lower temperatures, while the diquark condensation line at higher chemical potentials shifts to higher temperatures as the cutoff is increased. Increasing the UV cutoff further (to $2\Lambda'$ or $4\Lambda'$ in our case) leads to no significant changes, highlighting the convergence of the RGC scheme as the UV cutoff Λ grows well above any external scale.

This nicely demonstrates that cutoff artifacts, which are present when external parameters such as T and μ are near the scale Λ , are reduced as Λ increases, consistent with previous studies Refs. [29, 31, 73]. Similarly, in the mLPA truncation, we observe analogous improvements compared to the mean-field case, but no significant modification of the back-bending behavior at low temperatures. This suggests that the back-bending is not driven by cutoff artifacts, in agreement with Ref. [87].

VI. SUMMARY AND CONCLUSIONS

In this work, we present a comprehensive analysis of the phase structure of the QMD model and explore its relation to diquark two-point functions in the context of the Silver-Blaze property. Our study is based on a FRG approach with two main objectives. First, it incorporates bosonic fluctuations beyond the standard MFA, which we implemented in the (pseudo)scalar mesonic channel. Second, by employing the RG consistency, it enables a systematic removal of cutoff artifacts, which is important in color-superconducting models due to medium-induced divergences.

In agreement with previous quark-meson model studies, we find that the inclusion of the (pseudo)scalar mesonic fluctuations leads to significant modifications of the phase structure. The characteristic back-bending behavior of the chiral transition is still present but is strongly affected by the onset of diquark condensation. For sufficiently large diquark coupling, diquark condensation dominates the phase structure in both MFA and mLPA. In the latter, this is accompanied by a noticeable reduction of the back-bending, although it is not completely removed, as reflected, for example, in regions of negative entropy density.

For large diquark couplings, diquark condensation sets in below both the vacuum quark mass and the chiral transition in both MFA and mLPA. Since the diquark onset is of second order, the Silver-Blaze property implies a diquark pole mass below twice the vacuum quark mass. This is confirmed by an explicit calculation of the vacuum diquark two-point function in both MFA and mLPA. We therefore conclude that the observed reduction of the back-bending at large couplings is closely linked to the emergence of a finite diquark pole mass. Notably, while the diquark curvature mass is fixed to twice the vacuum quark mass by construction, the pole mass can deviate significantly from the curvature mass.

The present mean-field treatment of the diquark sector constitutes a first step towards an FRG description of the QMD model. A natural extension is the consistent inclusion of diquark fluctuations, which is expected to provide further insight into the origin of the reduced back-bending of the chiral transition line. At present, it remains unclear whether this reduction is primarily driven by diquark condensation or reflects an artefact of the present diquark truncation.

In conclusion, our study highlights the relevance of the vacuum diquark pole mass in understanding the phase structure of dense quark matter. Its value relative to the vacuum constituent quark mass can constrain the location of the diquark onset and the interplay between chiral symmetry breaking and color superconductivity. Since the Silver-Blaze property is exact in QCD, this connection between the diquark pole mass and the onset of color superconductivity is expected to remain robust in more complete FRG truncations and ultimately in full QCD. This motivates a first-principles determination of

the scalar diquark vacuum properties, for instance within lattice QCD, more advanced FRG truncations, or DSE approaches.

ACKNOWLEDGMENTS

We thank Michael Buballa, Christian Fischer, Hosein Gholami, Lutz Kiefer, Jan Pawłowski, Fabian Rennecke, Franz Sattler and Lorenz von Smekal for discussions. This work has been supported by the Helmholtz Graduate School for Hadron and Ion Research (HGS-HIRE) for FAIR, the GSI Helmholtzzentrum für Schwerionenforschung and the Deutsche Forschungsgemeinschaft (DFG, German Research Foundation) through the Collaborative Research Center TransRegio CRC-TR 211 “Strong-interaction matter under extreme conditions”.

DATA AVAILABILITY

The numerical data presented in all figures in this work are openly available in the ancillary files of the corresponding arXiv submission.

Appendix A: Regulator functions

Actual computation of the average action Γ_k requires the explicit specification of the generic regulator $R_k(p, q)$. A momentum-space representation of the flow allows to evaluate the functional traces for constant field configurations. The regulator should be chosen such that the analytic properties and symmetries of the underlying theory are respected, as emphasized in studies of regulator-scheme dependence and RG consistency [79, 86, 94]. This is achieved by choosing the same matrix structure as the kinetic term which respects the Lorentz, Dirac, color and flavor structure of the theory. The regulator function is matrix-valued and, depending on the field space, has diagonal entries for bosonic fields and symplectic ones for fermions.

We employ spatial three-dimensional flat regulators [95]. This choice of regulator does not affect the frequency component of the 4-momentum and enables the internal frequency integration, or Matsubara summation at finite temperature, of the flow equations explicitly. This is crucial for the analytic continuation of the two-point flow equations from imaginary to real frequencies, which is necessary for the analysis of the diquark pole mass. It is furthermore consistent with the Silver-Blaze property [79]. The breaking of Lorentz symmetry induced by three-dimensional regulator functions is small, well understood, and does not significantly affect the phase structure or two-point functions.

For bosonic fields, the regulators read in terms of the

dimensionless momentum ratio $x = \vec{p}^2/k^2$

$$R_{k,b}(\vec{p}^2) = \vec{p}^2 r_b(x) \quad (\text{A1})$$

with the dimensionless bosonic shape function

$$r_b(x) = (1/x - 1)\theta(1 - x) . \quad (\text{A2})$$

For fermionic fields,

$$R_{k,q}(\vec{p}) = i\vec{p} r_q(x) \quad (\text{A3})$$

the dimensionless fermionic shape function is given by

$$r_q(x) = (1/\sqrt{x} - 1)\theta(1 - x) . \quad (\text{A4})$$

Both shape functions $r_b(x)$ and $r_q(x)$ are related by

$$(1 + r_q(x))^2 = (1 + r_b(x)) , \quad (\text{A5})$$

which has been used in the flow Eq. (33). In field space, fermionic regulators always have a symplectic structure. For example, for our choice of the superfield, Eq. (18), the regulator matrix reads

$$R_k = \begin{pmatrix} 0 & i\vec{p}^\top r_q(x) & 0 & 0 & 0 \\ i\vec{p} r_q(x) & 0 & 0 & 0 & 0 \\ 0 & 0 & \vec{p}^2 r_b(x) & 0 & 0 \\ 0 & 0 & 0 & 0 & \vec{p}^2 r_b(x) \\ 0 & 0 & 0 & \vec{p}^2 r_b(x) & 0 \end{pmatrix} . \quad (\text{A6})$$

Appendix B: Quark propagator

In this appendix, we detail the inversion of the quark propagator $G_{q,k}^{-1}$ defined in Eq. (21), including its nontrivial color structure. Rather than employing the Nambu-Gor'kov formalism to invert the quark propagator, see e.g. Ref. [96], we adopt a more straightforward approach. The regularized inverse propagator at finite temperature and chemical potential in the field space $\Psi(p) = (q(p), \bar{q}(p))$ can be expressed in block-matrix form as

$$G_{q,k}^{-1}(p) = \begin{pmatrix} \Delta & G_0^{-1,\top} \\ \bar{G}_0^{-1} & \Delta^\dagger \end{pmatrix} . \quad (\text{B1})$$

The inverse free quark propagator with $m_q = g_\phi \sigma$ reads

$$G_0^{-1} = (i\nu_n - \mu)\gamma_4 + i\vec{p}_{\text{reg},q} + m_q , \quad (\text{B2})$$

and the gap matrices are defined as

$$\begin{aligned} \Delta &= i\Delta_{\text{gap}} C \gamma_5 \tau_2 \epsilon_3 , \\ \text{and } \Delta^\dagger &= -i\Delta_{\text{gap}} C \gamma_5 \tau_2 \epsilon_3 , \end{aligned} \quad (\text{B3})$$

where $\Delta_{\text{gap}} = g_\Delta \Delta$. The charged-conjugate inverse propagator follows from

$$\bar{G}_0^{-1}(p) = -G_0^{-1}(-p) . \quad (\text{B4})$$

For notational simplicity, color indices are suppressed in the propagator, and we use the shorthand $\epsilon_3 \equiv (\epsilon_3)_{\text{ab}} = \epsilon_{3\text{ab}}$.

This matrix can be inverted by means of the two sets of energy projection operators P_\pm and \bar{P}_\pm on positive and negative energy states of the free Dirac equation for massive quarks

$$P_\pm(\vec{p}) = \frac{1}{2} \left(\gamma_4 \pm \frac{i\vec{p} + m_q}{\epsilon_q(\vec{p})} \right) \gamma_4 , \quad (\text{B5})$$

and correspondingly for massive charge-conjugated antiquarks

$$\bar{P}_\pm(\vec{p}) = \frac{1}{2} \left(\gamma_4 \pm \frac{i\vec{p} - m_q}{\epsilon_q(\vec{p})} \right) \gamma_4 , \quad (\text{B6})$$

with $\epsilon_q(\vec{p}) = \sqrt{\vec{p}^2 + m_q^2}$.

Both sets of operators are hermitian, i.e., $P_\pm^\dagger = P_\pm$, and they fulfill the usual projection properties $P_\pm P_\pm = P_\pm$, $P_\pm P_\mp = 0$, and $P_+ + P_- = 1$ for the quark sector and similarly for the charge-conjugated antiquark sector \bar{P}_\pm . Since $\text{tr} P_\pm = \text{tr} \bar{P}_\pm = 2$, each energy projector corresponds to two spin orientations of the quark and of the charge-conjugated antiquark. The relations $\gamma_4 P_\pm \gamma_4 = \bar{P}_\mp$ and $\gamma_5 P_\pm \gamma_5 = \bar{P}_\pm$ determine the action of the Dirac matrices on the energy projectors, with γ_4 exchanging and γ_5 preserving the energy sectors. This guarantees that the pairing propagator couples the appropriate particle-hole components without inducing spurious mixing.

One then finds

$$G_0^{-1} = (i\nu_n + \epsilon_q^-) P_+ \gamma_4 + (i\nu_n - \epsilon_q^+) P_- \gamma_4 , \quad (\text{B7})$$

with $\epsilon_q^\pm = \epsilon_q \pm \mu$. Note that the inverse propagators, G_0^{-1} and \bar{G}_0^{-1} , depend on the regularized momenta $\vec{p}_{\text{reg},q}$ rather than on \vec{p} .

The full inverse quark propagator can be written as

$$\mathcal{G}_{q,k}^{-1} = T G_{q,k}^{-1} \quad \text{with} \quad T = \begin{pmatrix} 0 & 1 \\ 1 & 0 \end{pmatrix} , \quad (\text{B8})$$

where the matrix T provides a convenient rearrangement of the basis; the same results can be obtained without introducing T . The propagator can then be inverted straightforwardly [97], yielding

$$\mathcal{G}_{q,k} = \begin{pmatrix} G^+ & F^- \\ F^+ & G^{-\top} \end{pmatrix} , \quad (\text{B9})$$

with

$$[G^+]^{-1} = \bar{G}_0^{-1} - \Delta^\dagger G_0^\top \Delta , \quad (\text{B10})$$

$$[G^-]^{-1,\top} = G_0^{-1,\top} - \Delta \bar{G}_0 \Delta^\dagger , \quad (\text{B11})$$

$$F^+ = -G_0^\top \Delta G^+ , \quad (\text{B12})$$

$$F^- = -\bar{G}_0 \Delta^\dagger G^{-\top} . \quad (\text{B13})$$

The evaluation of Eqs. (B10) to (B13) relies on the color-space relation

$$(\epsilon_3)^2 = -P_{rg} = -\text{diag}(1, 1, 0), \quad (\text{B14})$$

which gives rise to the characteristic 2SC pairing structure. The transposed expressions in Dirac space can be simplified using $C\gamma_5(P_\pm\gamma_4)^\top C\gamma_5 = P_\pm\gamma_4$ and $C\gamma_5(\bar{P}_\pm\gamma_4)^\top C\gamma_5 = \bar{P}_\pm\gamma_4$.

One then finds

$$G^+ = G_\Delta P_{rg} + G_0 P_b, \quad (\text{B15})$$

$$G^- = \bar{G}_\Delta P_{rg} + \bar{G}_0 P_b, \quad (\text{B16})$$

$$F^+ = F^{-\dagger} = \Xi P_{rg}, \quad (\text{B17})$$

with the propagator in the blue sector, $P_b = \text{diag}(0, 0, 1)$, given by

$$G_0 = \frac{1}{i\nu_n - \epsilon_q^-} P_+\gamma_4 + \frac{1}{i\nu_n + \epsilon_q^+} P_-\gamma_4, \quad (\text{B18})$$

and in the red-green sector by

$$G_\Delta = \frac{i\nu_n + \epsilon_q^-}{(i\nu_n)^2 - E_q^-^2} P_+\gamma_4 + \frac{i\nu_n - \epsilon_q^+}{(i\nu_n)^2 - E_q^+^2} P_-\gamma_4. \quad (\text{B19})$$

Similar to the inverse propagators in Eq. (B1), the corresponding charge-conjugate propagators \bar{G}_0 and \bar{G}_Δ are related to G_0 and G_Δ via

$$\bar{G}_0(p) = -G_0(-p), \quad \text{and} \quad \bar{G}_\Delta(p) = -G_\Delta(-p). \quad (\text{B20})$$

Finally, the full inverted quark propagator $G_{q,k}$, as introduced in Eq. (25), can be obtained via the basis reordering transformation

$$G_{q,k} = \mathcal{G}_{q,k} T. \quad (\text{B21})$$

Appendix C: Initial UV parameters and numerical details

Here, we summarize the numerical input parameters used throughout this work. Within the RGC setup two ultraviolet cutoffs are employed. The standard UV cutoff is denoted by Λ' , while the RGC UV cutoff is taken as $\Lambda = 10\Lambda' = 6 \text{ GeV}$, unless stated otherwise.

	$b_1[\text{MeV}^2]$	g_Δ	$a_1[\text{MeV}^2]$	a_2	g_ϕ	$h[\text{MeV}^3]$	$\Lambda'[\text{MeV}]$
MFA	$(755.65)^2$	6	$(270.76)^2$	1.70	3.25	$(120.70)^3$	600
	$(712.16)^2$	5	"	"	"	"	"
	$(673.92)^2$	4	"	"	"	"	"
	$(642.65)^2$	3	"	"	"	"	"
LPA	$(746.32)^2$	6	$-(109.34)^2$	4.60	3.25	$(120.70)^3$	600
	$(704.27)^2$	5	"	"	"	"	"
	$(669.40)^2$	4	"	"	"	"	"
	$(640.31)^2$	3	"	"	"	"	"

Table II. Initial UV parameters used in the FRG and MFA analyses.

The initial flow parameters at the UV scale $\Lambda' = 600 \text{ MeV}$ are listed in Tab. II. As discussed in Sec. III B, the parameters in the (pseudo)scalar interaction channel, a_1 , a_2 , g_ϕ , and h , are fixed from vacuum phenomenology and are taken from Ref. [98]. The diquark mass parameter b_1 is adjusted for each value of the diquark coupling g_Δ such that the diquark curvature mass in the infrared satisfies $m_{\Delta,\text{curv}}^2 = (600 \text{ MeV})^2$.

With the input parameters specified above, the numerical determination of the chiral and diquark condensates is performed by solving the flow equation Eq. (38), on a one-dimensional σ grid using the finite-difference upwind scheme described in Ref. [99], for fixed values of Δ . The minimum in the σ direction,

$$\min_{\sigma} \{U_{k=0}(\sigma, \Delta) - h\sigma\}$$

is then minimized with respect to Δ .

The numerical calculations presented in this work were performed using the SciML ecosystem [100–102] within the Julia programming language [103], supplemented by selected algorithms from the SUNDIALS suite [104, 105]. All figures are produced using Makie.jl [106] and TikZ-Feynman [107].

- [1] K. Hebeler, Three-nucleon forces: Implementation and applications to atomic nuclei and dense matter, *Phys. Rept.* **890**, 1 (2021), arXiv:2002.09548 [nucl-th].
- [2] M. G. Alford, K. Rajagopal, and F. Wilczek, Qcd at finite baryon density: Nucleon droplets and color superconductivity, *Phys. Lett. B* **422**, 247 (1998), arXiv:hep-ph/9711395.
- [3] M. G. G. Alford, Color superconducting quark matter,

Ann. Rev. Nucl. Part. Sci. **51**, 131 (2001), arXiv:hep-ph/0102047.

- [4] M. G. Alford, A. Schmitt, K. Rajagopal, and T. Schäfer, Color superconductivity in dense quark matter, *Rev. Mod. Phys.* **80**, 1455 (2008), arXiv:0709.4635 [hep-ph].
- [5] K. Fukushima and T. Hatsuda, The phase diagram of dense qcd, *Rept. Prog. Phys.* **74**, 014001 (2011), arXiv:1005.4814 [hep-ph].

- [6] R. Anglani, R. Casalbuoni, M. Ciminale, N. Ippolito, R. Gatto, M. Mannarelli, and M. Ruggieri, Crystalline color superconductors, *Rev. Mod. Phys.* **86**, 509 (2014), [arXiv:1302.4264 \[hep-ph\]](#).
- [7] M. Buballa and S. Carignano, Inhomogeneous chiral condensates, *Prog. Part. Nucl. Phys.* **81**, 39 (2015), [arXiv:1406.1367 \[hep-ph\]](#).
- [8] W.-j. Fu, J. M. Pawłowski, and F. Rennecke, QCD phase structure at finite temperature and density, *Phys. Rev. D* **101**, 054032 (2020), [arXiv:1909.02991 \[hep-ph\]](#).
- [9] R. D. Pisarski and F. Rennecke, Signatures of Moat Regimes in Heavy-Ion Collisions, *Phys. Rev. Lett.* **127**, 152302 (2021), [arXiv:2103.06890 \[hep-ph\]](#).
- [10] W.-j. Fu, J. M. Pawłowski, R. D. Pisarski, F. Rennecke, R. Wen, and S. Yin, The qcd moat regime and its real-time properties, (2024), [arXiv:2412.15949 \[hep-ph\]](#).
- [11] T. F. Motta, M. Buballa, and C. S. Fischer, New tool to detect inhomogeneous chiral symmetry breaking, (2024), [arXiv:2411.02285 \[hep-ph\]](#).
- [12] A. Schmitt, Phases and properties of color superconductors, (2025), [arXiv:2511.07319 \[hep-ph\]](#).
- [13] J. M. Pawłowski, F. Rennecke, and F. R. Sattler, Inhomogeneous instabilities in high-density QCD, (2025), [arXiv:2512.20510 \[hep-ph\]](#).
- [14] A. Bazavov *et al.* (HotQCD), Chiral crossover in QCD at zero and non-zero chemical potentials, *Phys. Lett. B* **795**, 15 (2019), [arXiv:1812.08235 \[hep-lat\]](#).
- [15] S. Borsanyi, Z. Fodor, J. N. Guenther, R. Kara, S. D. Katz, P. Parotto, A. Pasztor, C. Ratti, and K. K. Szabo, Qcd crossover at finite chemical potential from lattice simulations, *Phys. Rev. Lett.* **125**, 052001 (2020), [arXiv:2002.02821 \[hep-lat\]](#).
- [16] L. Dini, P. Hegde, F. Karsch, A. Lahiri, C. Schmidt, and S. Sharma, Chiral phase transitions in three-flavor QCD from lattice QCD, *Phys. Rev. D* **105**, 034510 (2022), [arXiv:2111.12599 \[hep-lat\]](#).
- [17] Y. Namekawa, K. Kashiwa, H. Matsuda, A. Ohnishi, and H. Takase, Improving efficiency of the path optimization method for a gauge theory, *Phys. Rev. D* **107**, 034509 (2023), [arXiv:2210.05402 \[hep-lat\]](#).
- [18] G. Aarts *et al.*, Phase transitions in particle physics: Results and perspectives from lattice quantum chromodynamics, *Prog. Part. Nucl. Phys.* **133**, 104070 (2023), [arXiv:2301.04382 \[hep-lat\]](#).
- [19] C. S. Fischer, Qcd at finite temperature and chemical potential from dyson-schwinger equations, *Prog. Part. Nucl. Phys.* **105**, 1 (2019), [arXiv:1810.12938 \[hep-ph\]](#).
- [20] W.-j. Fu, QCD at finite temperature and density within the fRG approach: an overview, *Commun. Theor. Phys.* **74**, 097304 (2022), [arXiv:2205.00468 \[hep-ph\]](#).
- [21] N. Dupuis, L. Canet, A. Eichhorn, W. Metzner, J. M. Pawłowski, M. Tissier, and N. Wschebor, The nonperturbative functional renormalization group and its applications, *Phys. Rept.* **910**, 1 (2021), [arXiv:2006.04853 \[cond-mat.stat-mech\]](#).
- [22] C. S. Fischer and J. M. Pawłowski, Phase structure and observables at high densities from first principles QCD, (2026), [arXiv:2603.11135 \[hep-ph\]](#).
- [23] J. Braun, H. Gies, and J. M. Pawłowski, Quark confinement from color confinement, *Phys. Lett. B* **684**, 262 (2010), [arXiv:0708.2413 \[hep-th\]](#).
- [24] J. Braun, L. Fister, J. M. Pawłowski, and F. Rennecke, From Quarks and Gluons to Hadrons: Chiral Symmetry Breaking in Dynamical QCD, *Phys. Rev. D* **94**, 034016 (2016), [arXiv:1412.1045 \[hep-ph\]](#).
- [25] M. Mitter, J. M. Pawłowski, and N. Strodthoff, Chiral symmetry breaking in continuum QCD, *Phys. Rev. D* **91**, 054035 (2015), [arXiv:1411.7978 \[hep-ph\]](#).
- [26] A. K. Cyrol, L. Fister, M. Mitter, J. M. Pawłowski, and N. Strodthoff, Landau gauge Yang-Mills correlation functions, *Phys. Rev. D* **94**, 054005 (2016), [arXiv:1605.01856 \[hep-ph\]](#).
- [27] A. K. Cyrol, M. Mitter, J. M. Pawłowski, and N. Strodthoff, Nonperturbative quark, gluon, and meson correlators of unquenched qcd, *Phys. Rev. D* **97**, 054006 (2018), [arXiv:1706.06326 \[hep-ph\]](#).
- [28] J. Braun and B. Schallmo, From quarks and gluons to color superconductivity at supranuclear densities, *Phys. Rev. D* **105**, 036003 (2022), [arXiv:2106.04198 \[hep-ph\]](#).
- [29] J. Braun, M. Leonhardt, and J. M. Pawłowski, Renormalization group consistency and low-energy effective theories, *SciPost Phys.* **6**, 056 (2019), [arXiv:1806.04432 \[hep-ph\]](#).
- [30] J. O. Andersen and M. P. Nødtvedt, Color superconductivity in the two-flavor quark-meson diquark model, (2024), [arXiv:2408.12361 \[hep-ph\]](#).
- [31] H. Gholami, L. Kurth, U. Mire, M. Buballa, and B.-J. Schaefer, Renormalizing the Quark-Meson-Diquark Model, (2025), [arXiv:2505.22542 \[hep-ph\]](#).
- [32] J. O. Andersen and M. P. Nødtvedt, Pion condensation versus 2SC, speed of sound, and charge neutrality effects in the quark-meson diquark model, (2025), [arXiv:2502.10229 \[hep-ph\]](#).
- [33] J. O. Andersen and M. P. Nødtvedt, Quark-meson diquark model and color superconductivity in dense quark matter, (2026), [arXiv:2602.18256 \[hep-ph\]](#).
- [34] J. B. Kogut, M. A. Stephanov, and D. Toublan, On two color QCD with baryon chemical potential, *Phys. Lett. B* **464**, 183 (1999), [arXiv:hep-ph/9906346](#).
- [35] J. O. Andersen and T. Brauner, Phase diagram of two-color quark matter at nonzero baryon and isospin density, *Phys. Rev. D* **81**, 096004 (2010), [arXiv:1001.5168 \[hep-ph\]](#).
- [36] N. Strodthoff, B.-J. Schaefer, and L. von Smekal, Quark-meson-diquark model for two-color QCD, *Phys. Rev. D* **85**, 074007 (2012), [arXiv:1112.5401 \[hep-ph\]](#).
- [37] N. Khan, J. M. Pawłowski, F. Rennecke, and M. M. Scherer, The Phase Diagram of QC2D from Functional Methods, (2015), [arXiv:1512.03673 \[hep-ph\]](#).
- [38] N. J. Evans, S. D. H. Hsu, and M. Schwetz, Nonperturbative couplings and color superconductivity, *Phys. Lett. B* **449**, 281 (1999), [arXiv:hep-ph/9810514](#).
- [39] T. Schäfer and F. Wilczek, High density quark matter and the renormalization group in qcd with two and three flavors, *Phys. Lett. B* **450**, 325 (1999), [arXiv:hep-ph/9810509](#).
- [40] H. Gies and C. Wetterich, Renormalization flow of bound states, *Phys. Rev. D* **65**, 065001 (2002), [arXiv:hep-th/0107221](#).
- [41] W.-j. Fu, X. Luo, J. M. Pawłowski, F. Rennecke, R. Wen, and S. Yin, Hyper-order baryon number fluctuations at finite temperature and density, *Phys. Rev. D* **104**, 094047 (2021), [arXiv:2101.06035 \[hep-ph\]](#).
- [42] K. Fukushima, J. M. Pawłowski, and N. Strodthoff, Emergent hadrons and diquarks, *Annals Phys.* **446**, 169106 (2022), [arXiv:2103.01129 \[hep-ph\]](#).
- [43] J. Stoll, N. Zorbach, and J. Braun, Nonperturbative fluctuation effects of charged bosonic fields: A

- quark-diquark model study at nonzero density, (2025), [arXiv:2510.01066 \[hep-ph\]](#).
- [44] M. Leonhardt, M. Pospiech, B. Schallmo, J. Braun, C. Drischler, K. Hebeler, and A. Schwenk, Symmetric nuclear matter from the strong interaction, *Phys. Rev. Lett.* **125**, 142502 (2020), [arXiv:1907.05814 \[nucl-th\]](#).
- [45] J. Braun and B. Schallmo, Zero-temperature thermodynamics of dense asymmetric strong-interaction matter, *Phys. Rev. D* **106**, 076010 (2022), [arXiv:2204.00358 \[nucl-th\]](#).
- [46] J. Braun, Fermion Interactions and Universal Behavior in Strongly Interacting Theories, *J. Phys. G* **39**, 033001 (2012), [arXiv:1108.4449 \[hep-ph\]](#).
- [47] J. Braun, M. Leonhardt, and M. Pospiech, Fierz-complete njl model study iii: Emergence from quark-gluon dynamics, *Phys. Rev. D* **101**, 036004 (2020), [arXiv:1909.06298 \[hep-ph\]](#).
- [48] D. T. Son, Superconductivity by long range color magnetic interaction in high density quark matter, *Phys. Rev. D* **59**, 094019 (1999), [arXiv:hep-ph/9812287](#).
- [49] R. D. Pisarski and D. H. Rischke, Gaps and critical temperature for color superconductivity, *Phys. Rev. D* **61**, 051501 (2000), [arXiv:nucl-th/9907041](#).
- [50] M. Buballa, NJL model analysis of quark matter at large density, *Phys. Rept.* **407**, 205 (2005), [arXiv:hep-ph/0402234](#).
- [51] J. Berges, D. U. Jungnickel, and C. C. Wetterich, Two flavor chiral phase transition from nonperturbative flow equations, *Phys. Rev. D* **59**, 034010 (1999), [arXiv:hep-ph/9705474](#).
- [52] B.-J. Schaefer and J. Wambach, The Phase diagram of the quark meson model, *Nucl. Phys. A* **757**, 479 (2005), [arXiv:nucl-th/0403039](#).
- [53] B.-J. Schaefer and J. Wambach, Susceptibilities near the qcd (tri)critical point, *Phys. Rev. D* **75**, 085015 (2007), [arXiv:hep-ph/0603256](#).
- [54] F. Rennecke and B.-J. Schaefer, Fluctuation-induced modifications of the phase structure in (2+1)-flavor QCD, *Phys. Rev. D* **96**, 016009 (2017), [arXiv:1610.08748 \[hep-ph\]](#).
- [55] S. Resch, F. Rennecke, and B.-J. Schaefer, Mass sensitivity of the three-flavor chiral phase transition, *Phys. Rev. D* **99**, 076005 (2019), [arXiv:1712.07961 \[hep-ph\]](#).
- [56] K. Otto, M. Oertel, and B.-J. Schaefer, Nonperturbative quark matter equations of state with vector interactions, *Eur. Phys. J. ST* **229**, 3629 (2020), [arXiv:2007.07394 \[hep-ph\]](#).
- [57] E. Grossi, F. J. Ihssen, J. M. Pawłowski, and N. Wink, Shocks and quark-meson scatterings at large density, *Phys. Rev. D* **104**, 016028 (2021), [arXiv:2102.01602 \[hep-ph\]](#).
- [58] F. Ihssen, J. M. Pawłowski, F. R. Sattler, and N. Wink, Towards quantitative precision for QCD at large densities, (2023), [arXiv:2309.07335 \[hep-th\]](#).
- [59] C. Wetterich, Exact evolution equation for the effective potential, *Phys. Lett. B* **301**, 90 (1993), two identical pdf papers original 1993 and 2017, [arXiv:1710.05815 \[hep-th\]](#).
- [60] L. Gor'kov, Microscopic derivation of the ginzburg-landau equations in the theory of superconductivity, *Sov. Phys. JETP* **36(9)**, 1364 (1959).
- [61] Y. Nambu, Quasi-particles and gauge invariance in the theory of superconductivity, *Phys. Rev.* **117**, 648 (1960).
- [62] M. L. Bellac, *Thermal Field Theory*, Cambridge Monographs on Mathematical Physics (Cambridge University Press, 2011).
- [63] W.-j. Fu, X. Luo, J. M. Pawłowski, F. Rennecke, and S. Yin, Ripples of the QCD Critical Point, (2023), [arXiv:2308.15508 \[hep-ph\]](#).
- [64] M. Hess, F. Karsch, E. Laermann, and I. Wetzorke, Diquark masses from lattice QCD, *Phys. Rev. D* **58**, 111502 (1998), [arXiv:hep-lat/9804023](#).
- [65] M. Oettel, R. Alkofer, and L. von Smekal, Nucleon properties in the covariant quark diquark model, *Eur. Phys. J. A* **8**, 553 (2000), [arXiv:nucl-th/0006082](#).
- [66] P. Maris, Effective masses of diquarks, *Few Body Syst.* **32**, 41 (2002), [arXiv:nucl-th/0204020](#).
- [67] H. Gholami, U. Mire, F. Rennecke, B.-J. Schaefer, and S. Yin, (to be published) (2026).
- [68] B. J. Schaefer and M. Wagner, QCD critical region and higher moments for three flavor models, *Phys. Rev. D* **85**, 034027 (2012), [arXiv:1111.6871 \[hep-ph\]](#).
- [69] V. Skokov, B. Friman, E. Nakano, K. Redlich, and B.-J. Schaefer, Vacuum fluctuations and the thermodynamics of chiral models, *Phys. Rev. D* **82**, 034029 (2010).
- [70] J. M. Pawłowski, Aspects of the functional renormalisation group, *Annals Phys.* **322**, 2831 (2007), [arXiv:hep-th/0512261](#).
- [71] J. M. Pawłowski, M. M. Scherer, R. Schmidt, and S. J. Wetzel, Physics and the choice of regulators in functional renormalisation group flows, *Annals Phys.* **384**, 165 (2017), [arXiv:1512.03598 \[hep-th\]](#).
- [72] T. K. Herbst, M. Mitter, J. M. Pawłowski, B.-J. Schaefer, and R. Stiele, Thermodynamics of QCD at vanishing density, *Phys. Lett. B* **731**, 248 (2014), [arXiv:1308.3621 \[hep-ph\]](#).
- [73] H. Gholami, M. Hofmann, and M. Buballa, Renormalization-group consistent treatment of color superconductivity in the NJL model, (2024), [arXiv:2408.06704 \[hep-ph\]](#).
- [74] A. Koenigstein, M. J. Steil, N. Wink, E. Grossi, J. Braun, M. Buballa, and D. H. Rischke, Numerical fluid dynamics for FRG flow equations: Zero-dimensional QFTs as numerical test cases. I. The O(N) model, *Phys. Rev. D* **106**, 065012 (2022), [arXiv:2108.02504 \[cond-mat.stat-mech\]](#).
- [75] A. Koenigstein, M. J. Steil, N. Wink, E. Grossi, and J. Braun, Numerical fluid dynamics for FRG flow equations: Zero-dimensional QFTs as numerical test cases. II. Entropy production and irreversibility of RG flows, *Phys. Rev. D* **106**, 065013 (2022), [arXiv:2108.10085 \[cond-mat.stat-mech\]](#).
- [76] T. D. Cohen, Functional integrals for QCD at nonzero chemical potential and zero density, *Phys. Rev. Lett.* **91**, 222001 (2003), [arXiv:hep-ph/0307089](#).
- [77] G. Markó, U. Reinosa, and Z. Szép, Bose-Einstein condensation and Silver Blaze property from the two-loop Φ -derivable approximation, *Phys. Rev. D* **90**, 125021 (2014), [arXiv:1410.6998 \[hep-ph\]](#).
- [78] W.-j. Fu, J. M. Pawłowski, F. Rennecke, and B.-J. Schaefer, Baryon number fluctuations at finite temperature and density, *Phys. Rev. D* **94**, 116020 (2016), [arXiv:1608.04302 \[hep-ph\]](#).
- [79] J. Braun, T. Dörnfeld, B. Schallmo, and S. Töpfel, Renormalization group studies of dense relativistic systems, *Phys. Rev. D* **104**, 096002 (2021), [arXiv:2008.05978 \[hep-ph\]](#).
- [80] R.-A. Tripolt, L. von Smekal, and J. Wambach,

- Flow equations for spectral functions at finite external momenta, *Phys. Rev. D* **90**, 074031 (2014), [arXiv:1408.3512 \[hep-ph\]](#).
- [81] R. D. Pisarski and D. H. Rischke, Color superconductivity in weak coupling, *Phys. Rev. D* **61**, 074017 (2000), [arXiv:nucl-th/9910056](#).
- [82] K.-I. Aoki, H. Uoi, and M. Yamada, Functional renormalization group study of the nambu extendashjonaslasinio model at finite temperature and density in an external magnetic field, *Phys. Lett. B* **753**, 580 (2016), [arXiv:1507.02527 \[hep-ph\]](#).
- [83] J. Weyrich, N. Strodthoff, and L. von Smekal, Chiral mirror-baryon-meson model and nuclear matter beyond mean-field approximation, *Phys. Rev. C* **92**, 015214 (2015), [arXiv:1504.02697 \[nucl-th\]](#).
- [84] R.-A. Tripolt, B.-J. Schaefer, L. von Smekal, and J. Wambach, Low-temperature behavior of the quark-meson model, *Phys. Rev. D* **97**, 034022 (2018), [arXiv:1709.05991 \[hep-ph\]](#).
- [85] H. Zhang, D. Hou, T. Kojo, and B. Qin, Functional renormalization group study of the quark-meson model with ω meson, *Phys. Rev. D* **96**, 114029 (2017), [arXiv:1709.05654 \[hep-ph\]](#).
- [86] K. Otto, C. Busch, and B.-J. Schaefer, Regulator scheme dependence of the chiral phase transition at high densities, *Phys. Rev. D* **106**, 094018 (2022), [arXiv:2206.13067 \[hep-ph\]](#).
- [87] J. Stoll, N. Zorbach, L. Kiefer, F. Murgana, J. Braun, and D. H. Rischke, Analysis of regulator and cutoff artifacts in the phase diagram of the quark-meson model, (2026), [arXiv:2601.23005 \[hep-ph\]](#).
- [88] C. Konrad and O. Philipsen, From deconfinement to nuclear matter: mean-field approaches for effective polyakov loop theories of lattice qcd, (2025), [arXiv:2509.03172 \[hep-lat\]](#).
- [89] F. Ihssen and J. M. Pawłowski, Flowing fields and optimal rg-flows, (2023), [arXiv:2305.00816 \[hep-th\]](#).
- [90] I. A. Shovkovy and P. J. Ellis, Thermal conductivity of dense quark matter and cooling of stars, *Phys. Rev. C* **66**, 015802 (2002), [arXiv:hep-ph/0204132](#).
- [91] M. Osman, D. Hou, W. Wang, and H. Zhang, Functional renormalization group study of the quark-meson model with omega and rho vector mesons, (2024), [arXiv:2402.15474 \[hep-ph\]](#).
- [92] U. Mire and B.-J. Schaefer, (to be published) (2026).
- [93] A. J. Helmboldt, J. M. Pawłowski, and N. Strodthoff, Towards quantitative precision in the chiral crossover: masses and fluctuation scales, *Phys. Rev. D* **91**, 054010 (2015), [arXiv:1409.8414 \[hep-ph\]](#).
- [94] I. Balog, H. Chaté, B. Delamotte, M. Marohnic, and N. Wschebor, Convergence of Nonperturbative Approximations to the Renormalization Group, *Phys. Rev. Lett.* **123**, 240604 (2019), [arXiv:1907.01829 \[cond-mat.stat-mech\]](#).
- [95] D. F. Litim, Optimized renormalization group flows, *Phys. Rev. D* **64**, 105007 (2001), [arXiv:hep-th/0103195](#).
- [96] M. Huang, P.-f. Zhuang, and W.-q. Chao, Massive quark propagator and competition between chiral and diquark condensate, *Phys. Rev. D* **65**, 076012 (2002), [arXiv:hep-ph/0112124](#).
- [97] Z. G. Wang, S. L. Wan, and W. M. Yang, A New approach for calculating the Nambu-Gorkov propagator in color superconductivity theory, eprint (2005), [arXiv:hep-ph/0508302](#).
- [98] K. Otto, M. Oertel, and B.-J. Schaefer, Hybrid and quark star matter based on a nonperturbative equation of state, *Phys. Rev. D* **101**, 103021 (2020), [arXiv:1910.11929 \[hep-ph\]](#).
- [99] F. Ihssen, F. R. Sattler, and N. Wink, Numerical RG-time integration of the effective potential: Analysis and benchmark, *Phys. Rev. D* **107**, 114009 (2023), [arXiv:2302.04736 \[hep-th\]](#).
- [100] C. Rackauckas and Q. Nie, DifferentialEquations.jl—a performant and feature-rich ecosystem for solving differential equations in Julia, *Journal of Open Research Software* **5** (2017).
- [101] V. K. Dixit and C. Rackauckas, *Optimization.jl: A unified optimization package* (2023).
- [102] A. Pal, F. Holtorf, A. Larsson, T. Loman, F. Schaefer, Q. Qu, A. Edelman, C. Rackauckas, *et al.*, Nonlinearsolve.jl: High-performance and robust solvers for systems of nonlinear equations in julia, *arXiv preprint arXiv:2403.16341* (2024).
- [103] J. Bezanson, A. Edelman, S. Karpinski, and V. B. Shah, Julia: A fresh approach to numerical computing, *SIAM Review* **59**, 65 (2017).
- [104] D. J. Gardner, D. R. Reynolds, C. S. Woodward, and C. J. Balos, Enabling new flexibility in the SUNDIALS suite of nonlinear and differential/algebraic equation solvers, *ACM Transactions on Mathematical Software (TOMS)* **48**, 1 (2022).
- [105] A. C. Hindmarsh, P. N. Brown, K. E. Grant, S. L. Lee, R. Serban, D. E. Shumaker, and C. S. Woodward, SUNDIALS: Suite of nonlinear and differential/algebraic equation solvers, *ACM Transactions on Mathematical Software (TOMS)* **31**, 363 (2005).
- [106] S. Danisch and J. Krumbiegel, Makie.jl: Flexible high-performance data visualization for Julia, *Journal of Open Source Software* **6**, 3349 (2021).
- [107] J. Ellis, Tikz-feynman: Feynman diagrams with tikz, *Comput. Phys. Commun.* **210**, 103 (2017), [arXiv:1601.05437 \[hep-ph\]](#).